



HAL
open science

Thermo-hydro-mechanical modeling of artificial ground freezing taking into account the salinity of the saturating fluid

Haffsa Tounsi, Ahmed Rouabhi, Emad Jahangir

► **To cite this version:**

Haffsa Tounsi, Ahmed Rouabhi, Emad Jahangir. Thermo-hydro-mechanical modeling of artificial ground freezing taking into account the salinity of the saturating fluid. *Computers and Geotechnics*, 2020, 119, pp.103382. 10.1016/j.compgeo.2019.103382 . hal-02427099

HAL Id: hal-02427099

<https://minesparis-psl.hal.science/hal-02427099>

Submitted on 7 Mar 2022

HAL is a multi-disciplinary open access archive for the deposit and dissemination of scientific research documents, whether they are published or not. The documents may come from teaching and research institutions in France or abroad, or from public or private research centers.

L'archive ouverte pluridisciplinaire **HAL**, est destinée au dépôt et à la diffusion de documents scientifiques de niveau recherche, publiés ou non, émanant des établissements d'enseignement et de recherche français ou étrangers, des laboratoires publics ou privés.



Distributed under a Creative Commons Attribution - NonCommercial 4.0 International License

Thermo-Hydro-Mechanical modeling of artificial ground freezing taking into account the salinity of the saturating fluid

H. Tounsi^{a,*}, A. Rouabhi^a, E. Jahangir^a

^a*MINES ParisTech, PSL Research University, Centre de Géosciences, 35 rue St Honoré 77300 Fontainebleau, France*

Abstract

The modeling of Artificial Ground Freezing in geotechnical engineering applications has two main objectives, the first is the prediction of the extent of the frozen zone around the cooling sources (Thermo-Hydraulic models) and the second is the prediction of the ground's deformations and the site stability (Thermo-Hydro-Mechanical models). Reliable predictions require the consideration of unfavorable hydro-geological conditions such as high seepage velocities, ground heterogeneity and saline groundwater that may negatively influence the performance of AGF. The influence of the saturating fluid salinity on the THM behavior of the ground during freezing is the less documented point among the three and is therefore the subject of this paper. To this end, a fully coupled THM model considering the salinity effect has been derived. The formalism is completely thermodynamically consistent and introduces some simplifying assumptions, especially to describe phase change terms (capillary pressure and latent heat), in order to achieve a mathematical formulation that can be easily handled by computation software. Stress-free freezing laboratory tests carried out on specimens initially fully saturated with sodium chloride solutions at three different concentrations allowed to validate the proposed approach and to highlight some key mechanisms associated with the phase change of saline-saturated porous media.

Keywords: Artificial ground freezing; Phase change; Salinity; THMC coupling; Stress-free laboratory freezing tests; Numerical modeling

*Corresponding author

Email address: hafssa.tounsi@mines-paristech.fr (H. Tounsi)

1. Introduction

The rising population flow and road traffic create a growing demand for underground transportation infrastructure, all over the world (for e.g. subway extension projects in Paris and Beijing). Consequently, the risk of encountering unfavorable ground conditions like water-bearing soil or soft rock is becoming increasingly important. Artificial Ground Freezing is a technique that has proven to be effective in waterproofing and ensuring the stability of such weak grounds (Sophiaspoor tunnel in the Netherlands [10], Napoli underground metro stations [24, 32], Gongbei Tunnel in Hong Kong [19] and Nanjing metro in China [18]). It is then becoming a widely-used technique, not only in tunneling projects, but in a broad range of geotechnical applications like shaft sinking [34] and protection barriers of mineral deposits [35, 45]. However, caution must be taken in the presence of high groundwater velocities as the flow-generated heat slows down or even prevent the closure of the frozen barrier in some localized areas [33]. This point is fairly well documented; different validated thermo-hydraulic models exist and can be used to predict the closure time and the extent of the frozen area [28, 31, 43, 44, 53]. Another problematic issue is the groundwater salinity that notably modifies the freezing behavior of the soil. The freezing point depression [2, 46] is only one effect among many [30]. Nevertheless, there has been very little research attempting to extend the existing thermo-hydraulic models with phase change to the case of porous media saturated with an aqueous solution instead of pure water. Rouabhi et al. [30] recently proposed a fully coupled heat and mass transfer formulation taking into account the salinity of the saturation fluid and carried out laboratory freeze-thaw experiments to validate it. In addition to the freezing point depression, their model considered also the impact of salt concentration on the physical properties of the aqueous solution and the phase change equations of state, directly derived from thermodynamically consistent liquid and ice Gibbs potential functions. However, the effect of the presence of solutes in the saturation fluid on the ground deformation was not investigated. This brings us to the third and likely one of the most important issues of ground freezing: the ground deformation resulting from the pore water's expansion while freezing which could lead to the deterioration of adjacent

structures.

When the ground subjected to freezing is frost-susceptible such as clay, silt, clayey sand and silty sand, the water migrating by capillary action from unfrozen regions to the frozen front forms ice lenses that produce a ground surface heave [37]. Literature has extensively investigated these phenomena and two approaches of thermo-hydro-mechanical modeling of ground freezing could be distinguished: capillary models [8, 26, 53] and frozen-fringe models [22, 38, 52]. Both approaches have their strengths and weaknesses and their capabilities to reproduce the behavior of the ground could be assessed only through experimental verification. The frozen-fringe models, on the contrary of capillary models, successfully capture the formation of discrete ice lenses in fine-grained soils but haven't been extended yet into three dimensions. Their verification is often carried out using one-dimensional long frost heave experiments [49]. The capillary models framework is more adapted to the simulation of rapid uniform freezing laboratory tests [8, 50] and at higher *in situ* overburden pressure conditions where ice lenses cannot form [40]. Again, the common shortcoming of the models of both categories, cited above, consists in neglecting the effects of the presence of solutes in the pore water. Recently, there has been an increasing interest in the behavior of saline soil among researchers concerned about the damage to buildings and infrastructure foundations resulting from the frost heave of sulfate saline soil in permafrost regions [23, 29, 48, 49]. In these works, the effects of the thermo-hydro-mechanical and chemical coupling were studied mainly through laboratory experiments consisting of cycles of uniaxial freezing and thawing for a single value of solute concentration. The theoretical framework, when provided, suffered from the lack of thermodynamic consistency and from unclear methodology, and required additional experimental verification regarding the freezing conditions, the type of the saturating fluid and the values of salt content.

To fill this gap, this paper proposes a coupled thermo-hydro-mechanical and chemical (THMC) model of ground freezing that falls into the category of capillary models for the reasons cited above in relation with the type of conducted experiments. The phase change fronts are tracked using the liquid saturation degree function, and the stress state of the ground is characterized through the concept of effective stress. Based on the literature men-

tioned above, the thermodynamics of phase change is recalled and the simplifications usually used to derive the expression of the capillary pressure are reviewed in order to take account of the liquid pressure effect. The paper is structured as follows: in Section 2 the balance and constitutive equations are derived within the theory of porous media, and in Section 3 the modeling formalism is validated against stress-free freezing laboratory experiments performed on limestone specimens initially fully saturated with sodium chloride solutions at various concentrations.

Nomenclature

Main symbols

| | |
|--------------------|-------------------------------------------------------------------------------|
| ρ^α | apparent density of phase α |
| ρ_α | density of phase α |
| ν_α | specific volume of phase α |
| $\Delta\nu_w$ | difference between partial specific volumes of water in ice and liquid phases |
| $C_{p\alpha}$ | heat capacity at constant pressure of phase α |
| ρC_p | volumetric heat capacity of the porous medium |
| Λ_α | thermal conductivity of phase α |
| Λ | thermal conductivity of the porous medium |
| k_0 | intrinsic permeability |
| k_r | relative permeability of phase λ |
| η_λ | dynamic viscosity of phase λ |
| D_λ | diffusivity coefficient of salt in phase λ |
| $\vec{\psi}$ | conductive heat flux vector |
| \vec{V} | filtration velocity of phase λ |
| \vec{J} | diffusion velocity vector of salt in phase λ |
| $\hat{\pi}^\gamma$ | mass rate of ice formation |
| h_α | specific enthalpy of phase α |
| g_α | specific Gibbs free energy of phase α |

| | |
|---------------------------------------|------------------------------------------------------------------------------------------------------------|
| Δh_w | latent heat of water phase change/ difference between partial enthalpies of water in ice and liquid phases |
| $L_{\lambda\gamma}$ | latent heat of phase change on the coexistence curve |
| $\mu_{w\lambda}$ | chemical potential of water in phase λ |
| μ_γ | chemical potential of ice |
| c | salt concentration in phase λ |
| c_{sat} | salt concentration at saturation |
| n | porosity |
| n_α | volume fraction of phase α |
| p_α | pressure of phase α |
| ϖ | equivalent pore pressure |
| $p_{\lambda\gamma}$ | coexistence pressure at thermodynamic equilibrium between λ and γ |
| p_c | capillary pressure |
| S_λ | liquid saturation degree |
| T | temperature |
| $T_{\lambda\gamma}$ | coexistence temperature at thermodynamic equilibrium between λ and γ |
| $\underline{\underline{1}}$ | second order unit tensor |
| $\underline{\underline{\sigma}}$ | total stress tensor |
| $\underline{\underline{\varepsilon}}$ | total strain tensor |
| \vec{u} | displacement vector |
| ε_v | volumetric strain |
| \mathbf{A} | drained linear thermal expansion coefficient |
| B | Biot coefficient |
| (\mathbf{E}_0, ν_0) | Young's modulus and Poisson's ratio of the material in the nonfrozen state |
| (\mathbf{E}_f, ν_f) | Young's modulus and Poisson's ratio of the material in the fully frozen state |

Subscripts or superscripts

σ solid phase

λ liquid phase

γ ice
 s salt
 w water

2. Theoretical framework

We consider an isotropic porous medium fully saturated with an aqueous solution and subjected to freezing. It consists of a solid skeleton phase σ , a liquid phase λ and an ice phase γ . The liquid phase is comprised of two components: water w and sodium chloride s . Ice is a single-component solid phase exchanging matter with the liquid phase; it is assumed to follow the movement of the solid skeleton phase σ and to behave as a fluid phase endowed with its own pressure and temperature. In what follows, T is the absolute temperature of all the phases (local thermal equilibrium assumption), n is the Eulerian porosity of the porous medium ~~and c is the mass concentration of salt s in liquid phase λ~~ . For each phase $\alpha = (\lambda, \gamma)$, p_α denotes its pressure, \vec{v}_α ~~its macroscopic velocity~~, ρ_α its density, $\nu_\alpha = 1/\rho_\alpha$ its specific volume, n_α its volume fraction, ~~$\rho^\alpha = \rho_\alpha n_\alpha$ its apparent density~~ and $S_\alpha = n_\alpha/n$ its saturation degree, with $S_\lambda + S_\gamma = 1$. For phase σ , $n_\sigma = 1 - n$ is its volume fraction and $\rho^\sigma = \rho_\sigma n_\sigma$ its apparent density. For each function $\varphi(\vec{x}, t)$ attached to the porous medium, $\dot{\varphi} = \partial_t \varphi + \vec{v}_\sigma \cdot \vec{\nabla} \varphi$ denotes its time derivative following the motion of solid skeleton phase σ . The mechanical behavior is assumed to be elastic and the small deformation assumption is adopted.

2.1. Balance equations

In this section, mass, energy and momentum balance equations are derived, ~~by applying the volume averaging method to the pore scale balance equations, as can be found in [17, 47] and by~~ taking the motion of solid phase σ as a reference.

2.1.1. Mass balance equation

A local conservative form of the mass balance equation of a component k of a fluid phase α at the pore scale can be written as follows:

$$\partial_t (\rho_\alpha c_{k\alpha}) + \overrightarrow{\nabla} \cdot (\rho_\alpha c_{k\alpha} \overrightarrow{v}_{k\alpha}) = 0 \quad (1)$$

where $c_{k\alpha}$ is the mass concentration of the component k in the phase α and $\overrightarrow{v}_{k\alpha}$ is the macroscopic velocity vector of the component k .

When applying the volume averaging method, the apparent density $\rho^\alpha = n_\alpha \rho_\alpha$ is introduced, and the following macroscopic mass balance equation of the component k can be obtained:

$$\partial_t (\rho^\alpha c_{k\alpha}) + \overrightarrow{\nabla} \cdot (\rho^\alpha c_{k\alpha} \overrightarrow{v}_{k\alpha}) = \hat{\pi}_k^\alpha \quad (2)$$

where the mass provided by chemical reactions has been neglected and where $\hat{\pi}_k^\alpha$ is the amount of mass provided to phase α due to the interfacial exchanges of the component k , such as $\sum_\alpha \hat{\pi}_k^\alpha = 0$ and $\sum_k \hat{\pi}_k^\alpha = \hat{\pi}^\alpha$, which represents the total mass of all the components that are exchanged at the interfaces with the phase α .

By introducing the diffusion velocity $\overrightarrow{J}_k^\alpha = n_\alpha c_{k\alpha} (\overrightarrow{v}_{k\alpha} - \overrightarrow{v}_\alpha)$, that describes the relative movement of the component k with respect to phase α , and the filtration velocity $\overrightarrow{V}^\alpha = n_\alpha (\overrightarrow{v}_\alpha - \overrightarrow{v}_\sigma)$, that describes the relative movement of phase α with respect to phase σ , and by using a lagrangian time derivative, the following mass balance equation of the component k can be deduced:

$$(\rho^\alpha \dot{c}_{k\alpha}) + (\rho^\alpha c_{k\alpha}) \dot{J}/J + \overrightarrow{\nabla} \cdot (\rho_\alpha c_{k\alpha} \overrightarrow{V}^\alpha + \rho_\alpha \overrightarrow{J}_k^\alpha) = \hat{\pi}_k^\alpha \quad (3)$$

where J is the Jacobian of the solid transformation. The hypothesis of small deformations entails that $\dot{J} = J \dot{\varepsilon}_v$, with $\varepsilon_v = \text{tr}(\underline{\underline{\varepsilon}})$ the volumetric component of the linearized strain tensor $\underline{\underline{\varepsilon}} = (\underline{\underline{\nabla}} \overrightarrow{u} + {}^t \underline{\underline{\nabla}} \overrightarrow{u})/2$, represented by the symmetric part of the gradient of the solid displacement vector \overrightarrow{u} .

Note that by summing Equation 3 for all the components of a phase α , the mass balance equation of the latter can be obtained:

$$\dot{\rho}^\alpha + \rho^\alpha \dot{\varepsilon}_v + \overrightarrow{\nabla} \cdot (\rho_\alpha \overrightarrow{V}^\alpha) = \hat{\pi}^\alpha \quad (4)$$

In our case, since ice phase is assumed to follow the movement of the solid skeleton ($\vec{V}^\gamma = \vec{0}^\gamma$) and the liquid phase λ contains only two components, water w and salt s, only one filtration velocity, one mass concentration and one diffusion velocity are required to formulate the problem to be solved. Hence, the notations will be simplified by setting: $\vec{V} = \vec{V}^\lambda$, $\vec{J} = \vec{J}_s^\lambda$ and $c = c_{s\lambda}$.

By using Equation 4, the following mass balance equations of phases λ and γ can be deduced: The mass balance equations of the phases λ and γ can be written in the following form:

$$\dot{\rho}^\lambda + \rho^\lambda \dot{\varepsilon}_v + \vec{\nabla} \cdot (\rho_\lambda \vec{V}) = \hat{\pi}^\lambda \quad (5)$$

$$\dot{\rho}^\gamma + \rho^\gamma \dot{\varepsilon}_v = \hat{\pi}^\gamma \quad (6)$$

where $\varepsilon_v = \text{tr}(\underline{\underline{\varepsilon}})$ is the volumetric component of the linearized strain tensor $\underline{\underline{\varepsilon}} = (\underline{\underline{\nabla}} \vec{u} + {}^t \underline{\underline{\nabla}} \vec{u})/2$, represented by the symmetric part of the gradient of the solid displacement vector \vec{u} ; $\hat{\pi}^\alpha$ is the amount of mass exchanged by phase α during phase change of water w, such as $\hat{\pi}^\lambda + \hat{\pi}^\gamma = 0$, and \vec{V} is the filtration velocity of the liquid phase λ .

Where $\hat{\pi}^\gamma = -\hat{\pi}^\lambda$ is the amount of mass provided to phase γ by the phase change of the water w.

We can get rid of the exchanged mass term by summing Equations (5) and (6). The mass balance equation of the two phases λ and γ can therefore be written as follows: The mass balance equation of the two phases λ and γ , obtained by summing Equations (5) and (6), can therefore be written as follows:

$$\dot{\rho}^\lambda + \dot{\rho}^\gamma + (\rho^\lambda + \rho^\gamma) \dot{\varepsilon}_v + \vec{\nabla} \cdot (\rho_\lambda \vec{V}) = 0 \quad (7)$$

By using Equation 3 and 5, with $\hat{\pi}_s^\lambda = 0$ since salt is not exchanged between phases, the following mass balance equation of salt s can be deduced is given by [30]:

$$\rho^\lambda \dot{c} + \rho_\lambda \vec{V} \cdot \vec{\nabla} c + \vec{\nabla} \cdot (\rho_\lambda \vec{J}) = \hat{\pi}^\gamma c \quad (8)$$

where \vec{J} is the diffusive velocity of salt in phase λ .

2.1.2. Heat equation

The heat balance equation can be written as follows [30]:

$$\rho C_p \dot{T} + \rho_\lambda C_{p\lambda} \vec{V} \cdot \vec{\nabla} T = -\vec{\nabla} \cdot \vec{\psi} - \hat{\pi}^\gamma \Delta h_w \quad (9)$$

with

$$\rho C_p = \sum_{\alpha} \rho^{\alpha} C_{p\alpha} \quad (10)$$

and

$$\Delta h_w(p_\lambda, p_\gamma, T, c) = h_\gamma - h_\lambda + c \partial_c h_\lambda \quad (11)$$

where $C_{p\alpha}$ denotes the heat capacity at constant pressure of phase α , $\vec{\psi}$ is the surface density of the amount of heat exchanged by conduction, $h_\gamma(p_\gamma, T)$ and $h_\lambda(p_\lambda, T, c)$ are the enthalpies of the ice and the liquid phases, respectively, and Δh_w is the latent heat of water phase change.

2.1.3. Momentum balance

If the inertial terms are neglected, the equation of balance of momentum reads:

$$\vec{\nabla} \cdot \underline{\underline{\sigma}} + \rho \vec{g} = \vec{0} \quad (12)$$

where the tensor $\underline{\underline{\sigma}}$ stands for the total stress tensor acting on both solid and fluid phases, $\rho = \sum_{\alpha} \rho^{\alpha}$ is the mass density of the porous medium and \vec{g} is the gravitational acceleration vector.

In macroscopic approaches, the water-ice interfaces are usually tracked using the water saturation degree function S_λ , equal to one in liquid saturated regions. Consequently, the balance between the pressure jump across these interfaces and the surface tension forces could be expressed through a macroscopic relationship between the pressure difference, the temperature, the salt concentration and the liquid saturation degree S_λ , as follows:

$$S_\lambda = \mathcal{S}(p_c, T, c) \quad (13)$$

where $p_c = p_\gamma - p_\lambda$ is the pressure difference across the interface $\lambda\gamma$, called the capillary pressure and \mathcal{S} is an empirical function that has been widely investigated in literature [3, 4,

11, 12, 21, 36, 39]. This latter could ideally be determined through one of the experimental methods used in the references cited above or otherwise via a back analysis of laboratory [30] or *in situ* measurements [40, 45].

2.2. Constitutive equations

To sum up, the set of partial differential equations to be solved is the following:

$$\left\{ \begin{array}{l} \dot{\rho}^\gamma + \rho^\gamma \dot{\varepsilon}_v = \hat{\pi}^\gamma \\ \dot{\rho}^\lambda + \dot{\rho}^\gamma + (\rho^\lambda + \rho^\gamma) \dot{\varepsilon}_v + \vec{\nabla} \cdot (\rho_\lambda \vec{V}) = 0 \\ \rho^\lambda \dot{c} - c(\dot{\rho}^\gamma + \rho^\gamma \dot{\varepsilon}_v) + \rho_\lambda \vec{V} \cdot \vec{\nabla} c + \vec{\nabla} \cdot (\rho_\lambda \vec{J}) = 0 \\ \rho C_p \dot{T} + \Delta h_w (\dot{\rho}^\gamma + \rho^\gamma \dot{\varepsilon}_v) + \rho_\lambda C_{p\lambda} \vec{V} \cdot \vec{\nabla} T + \vec{\nabla} \cdot \vec{\psi} = 0 \\ \vec{\nabla} \cdot \underline{\underline{\sigma}} + \rho \vec{g} = \vec{0} \end{array} \right. \quad (14)$$

where ρC_p and S_λ are given by Equations 10 and 13, respectively.

The System 14 is composed of four scalar equations and one vector equation. At the same time, it introduces eleven scalar unknowns: T , c , p_λ , p_γ , n , ρ_λ , ρ_γ , $C_{p\lambda}$, $C_{p\gamma}$, Δh_w and $\hat{\pi}^\gamma$, four vector unknowns: \vec{u} , \vec{V} , \vec{J} and $\vec{\psi}$ and one tensor unknown $\underline{\underline{\sigma}}$. The number of unknowns being greater than the number of equations, System 14 needs then to be supplemented, in addition to the thermodynamic equations of state, by some complementary equations (constitutive equations) to express the secondary unknowns ($\hat{\pi}^\gamma, \vec{V}, \vec{J}, \vec{\psi}$), the porosity evolution equation and the constitutive law of the solid matrix.

2.2.1. Complementary equations

With regard to the term $\hat{\pi}^\gamma$, resulting from the matter exchange at the interface $\lambda\gamma$, we assume, for the sake of simplicity, that the chemical equilibrium of the component w at the interface $\lambda\gamma$ is reached instantaneously and without any dissipation. Consequently, the chemical potentials of the ice phase and of water in phase λ are equal, as follows:

$$\mu_\gamma(p_\gamma, T) = \mu_{w\lambda}(p_\lambda, T, c) \quad (15)$$

Ice, being a pure phase, its chemical potential μ_γ is independent of the concentration c and equal to its Gibbs specific free energy g_γ . The chemical potential of water in phase λ is $\mu_{w\lambda} = g_\lambda - c \partial_c g_\lambda$.

Previous works [30, 31, 42] presented elaborate mathematical developments of Equation 15 in both cases of saline and non-saline porous media, that entailed the following relation:

$$\forall(p_\lambda, p_\gamma, T, c) : \int_{p_{\lambda\gamma}(T,c)}^{p_\gamma} \nu_\gamma(x, T) dx = \int_{p_{\lambda\gamma}(T,c)}^{p_\lambda} (\nu_\lambda - c\partial_c \nu_\lambda)(x, T, c) dx \quad (16)$$

with $p_{\lambda\gamma}$ being the coexistence pressure at the thermodynamic equilibrium between λ and γ . This equation allows the determination of the capillary pressure p_c as a function of (p_λ, T, c) .

As in most of the literature about porous media, the secondary unknowns \vec{V} , \vec{J} and $\vec{\psi}$ are expressed, respectively, by the generalized Darcy's law, Fick's law and Fourier's law, as follows:

$$\vec{V} = -\frac{k_\lambda}{\eta_\lambda} (\vec{\nabla} p_\lambda - \rho_\lambda \vec{g}'), \quad \vec{J} = -D_\lambda \vec{\nabla} c, \quad \vec{\psi} = -\Lambda \vec{\nabla} T \quad (17)$$

where k_λ is the intrinsic permeability associated to the filtration of phase λ through the solid skeleton, η_λ is the dynamic viscosity of the liquid phase λ , D_λ is the diffusivity of salt s into phase λ and Λ is the thermal conductivity of the porous medium. In order to allow the consideration of the effects of the ice phase formation on preventing the liquid phase flow, the four scalars may depend on the saturation degree in addition to the thermodynamic state variables (p_λ, T, c) .

2.2.2. Mechanical constitutive law and porosity evolution

To express the stress-strain relationship, the concept of effective stress [6] is used and a partition of the total strain rate tensor $\dot{\underline{\underline{\epsilon}}}$ into an elastic component $\dot{\underline{\underline{\epsilon}}}^e$, a non-elastic one $\dot{\underline{\underline{\epsilon}}}^{ne}$ and a thermal component $\mathbf{A}\dot{T}\underline{\underline{1}}$ is adopted. This entails the following equation:

$$\dot{\underline{\underline{\epsilon}}} + B\dot{\varpi}\underline{\underline{1}} = \underline{\underline{\mathbf{H}}} : \left(\dot{\underline{\underline{\epsilon}}} - \dot{\underline{\underline{\epsilon}}}^{ne} - \mathbf{A}\dot{T}\underline{\underline{1}} \right) \quad (18)$$

where \mathbf{A} is the drained linear thermal expansion coefficient, B is the Biot coefficient, ϖ is the equivalent pore pressure and $\underline{\underline{\mathbf{H}}}$ is the drained Hooke's elasticity tensor.

The Biot coefficient B is often approximated using the following expression:

$$B = 1 - \frac{K}{K_\sigma} \quad (19)$$

where \mathbf{K} and \mathbf{K}_σ are the drained and solid bulk moduli, respectively.

The pore pressure ϖ is assumed to be a function of the pressure p_λ and the capillary pressure p_c and is expressed as follows [40]:

$$\varpi = p_\lambda + \int_0^{p_c} (1 - S_\lambda(x)) dx \quad (20)$$

Classical mechanical tests on frozen and unfrozen materials in literature have shown that the Young's modulus and the Poisson's ratio are dependent upon temperature. To account for this property, equivalent Young's modulus and Poisson's ratio (\mathbf{E} , $\boldsymbol{\nu}$) of the mixture [16, 53] are considered, as follows:

$$\begin{aligned} \mathbf{E} &= S_\lambda \mathbf{E}_0 + (1 - S_\lambda) \mathbf{E}_f \\ \boldsymbol{\nu} &= S_\lambda \boldsymbol{\nu}_0 + (1 - S_\lambda) \boldsymbol{\nu}_f \end{aligned} \quad (21)$$

where $(\mathbf{E}_0, \boldsymbol{\nu}_0)$ and $(\mathbf{E}_f, \boldsymbol{\nu}_f)$ are the Young's moduli and the Poisson's ratios of the material in the nonfrozen state and the fully frozen state, respectively.

To determine partial porosities of λ and γ phases, the following evolution equation of the total porosity is used [7]:

$$\dot{n} = (B - n) \left(\dot{\varepsilon}_v - 3\mathbf{A}\dot{T} + \frac{1 - B}{\mathbf{K}} (S_\lambda \dot{p}_\lambda + (1 - S_\lambda) \dot{p}_\gamma) \right) - B \dot{\varepsilon}_v^{\text{ne}} \quad (22)$$

In this paper, the non-elastic strain tensor is assumed to be zero. Indeed, numerical simulations presented in Section 3.2 have shown that a non-linear elastic model is sufficient to explain the measured freezing-induced strains.

2.2.3. Thermodynamic equations of state

The density and the thermal capacity of the solid skeleton phase are assumed to be constant. Consequently, in this subsection and the next one, the α subscript refers to phase λ or phase γ .

In order to build a thermodynamically consistent model, the state functions of each phase α should be derived from its thermodynamic potential and its partial derivatives. The thermodynamic state independent variables being (p_α, T, c) , the thermodynamic potential

chosen in this work is thus the Gibbs specific free energy g_α . The specific volumes ν_α , the thermal capacities $C_{p\alpha}$ and the enthalpies h_α can then be expressed as follows [14]:

$$\begin{cases} \dot{\nu}_\alpha/\nu_\alpha = \chi_{T\alpha}\dot{T} - \chi_{p\alpha}\dot{p}_\alpha + \chi_{s\alpha}\dot{c} \\ \chi_{T\alpha} = \partial_{p_\alpha T}^2 g_\alpha/\nu_\alpha, \quad \chi_{p\alpha} = -\partial_{p_\alpha}^2 g_\alpha/\nu_\alpha, \quad \chi_{s\alpha} = -\partial_{p_\alpha c}^2 g_\alpha/\nu_\alpha \\ C_{p\alpha} = -T\partial_{T^2}^2 g_\alpha, \quad h_\alpha = g_\alpha - T\partial_T g_\alpha \end{cases} \quad (23)$$

where $\chi_{T\alpha}$ and $\chi_{p\alpha}$ are respectively the isobaric thermal expansion coefficient and the isothermal compressibility of phase α . The coefficient $\chi_{s\alpha}$ accounts for the effect of the variation of salt concentration at constant pressure and temperature.

The condition of water chemical equilibrium formulated in Equation (15) combined to the above expression of enthalpy leads to the following expression of phase change latent heat Δh_w :

$$\Delta h_w(p_\lambda, p_\gamma, T, c) = L_{\lambda\gamma}(T, c) - T \int_{p_{\lambda\gamma}(T, c)}^{p_\gamma} \partial_T \nu_\gamma(x, T) dx + T \int_{p_{\lambda\gamma}(T, c)}^{p_\lambda} \partial_T (\nu_\lambda - c\partial_c \nu_\lambda)(x, T, c) dx \quad (24)$$

where $L_{\lambda\gamma}(T, c) = \Delta h_w(p_{\lambda\gamma}(T, c), p_{\lambda\gamma}(T, c), T, c)$ denotes the latent heat of the solid-liquid water phase change within the domain of chemical equilibria such as $p_\lambda = p_\gamma = p_{\lambda\gamma}(T, c)$. Its expression is obtained by derivating Equation 15 with respect to T , which leads to:

$$L_{\lambda\gamma}(T, c) = T\Delta\nu_w(p_{\lambda\gamma}(T, c), T, c)\partial_T p_{\lambda\gamma}(T, c) \quad (25)$$

where $\Delta\nu_w(p, T, c) = \nu_\gamma(p, T) - (\nu_\lambda - c\partial_c \nu_\lambda)(p, T, c)$.

In this paper, the Gibbs free energy of aqueous NaCl solution g_λ is given by Archer and Carter [1] and the Gibbs function of ice g_γ is defined by Feistel and Wagner [13].

2.2.4. Simplification of equations of state

By using the rigorous mathematical expressions of the Gibbs potential functions mentioned in the previous subsection to derive the state laws, the resulting mathematical formalism would be complex and heavy to integrate in numerical codes. For this reason, some simplifying assumptions need to be introduced to reduce the computational load of the formalism without affecting its reliability and accuracy.

First of all, let's assume that the specific volumes of the liquid and ice phases are pressure-independent: $\nu_\lambda(p, T, c) = \nu_\lambda(p_0, T, c)$ and $\nu_\gamma(p, T) = \nu_\gamma(p_0, T)$. Accordingly, the equality 16 becomes:

$$p_c = \rho_\gamma(T)\Delta\nu_w(T, c)(p_{\lambda\gamma}(T, c) - p_\lambda) \quad (26)$$

Secondly, if a first order approximation around the reference state $(p_0, T_0(c))$ is used for $p_{\lambda\gamma}$ (see [30]), the pressure at the thermodynamic equilibrium between λ and γ can be written as:

$$p_{\lambda\gamma}(T, c) = p_0 + p'_{\lambda\gamma}(c)(T - T_0(c)) \quad (27)$$

The term $(p_{\lambda\gamma}(T, c) - p_\lambda)$ in Equation 26 can be rewritten as $(p_{\lambda\gamma}(T, c) - p_{\lambda\gamma}(T_{\lambda\gamma}(p_\lambda, c)))$, with $T_{\lambda\gamma}$ the coexistence temperature at the thermodynamic equilibrium between λ and γ . Thus, by making use of Equation 27, Equation 26 becomes:

$$p_c = \rho_\gamma(T)\Delta\nu_w(T, c)p'_{\lambda\gamma}(c)(T - T_{\lambda\gamma}(p_\lambda, c)) \quad (28)$$

The variation of $T_{\lambda\gamma}(p_\lambda, c)$ with p_λ is often neglected compared to its variation with c (see [8, 30, 44]). To investigate the validity of this hypothesis, we represent in Figure 1 the two-phase coexistence curve $T_{\lambda\gamma}$, numerically obtained from the equality 15 for $T = T_{\lambda\gamma}$ and $p_\lambda = p_\gamma = p$, as a function of c ranging from 0 to 0.25 (saturation concentration of NaCl aqueous solutions) for four values of p . These latter were chosen on the basis of a literature review on hydraulic pressure values that could be reached during the freezing of an initially fully saturated geomaterial. Indeed, the magnitude of p depends on the cooling conditions, drained or undrained, on the nature of the liquid saturating the pores and on the hydro-mechanical parameters of the material (permeability, Young's modulus, etc). The figure clearly shows that the difference between the reference curve $T_{\lambda\gamma}(p_0, c)$ and the other curves becomes significant for higher values of liquid pressure. Therefore, the assumption of replacing $T_{\lambda\gamma}(p_\lambda, c)$ by $T_0(c)$ is not always valid and is not retained in this work. The expression of capillary pressure is then as follows:

$$p_c = -\rho_\gamma(T)\Delta\nu_w(T, c)(p_\lambda - p_0) + \rho_\gamma(T)\Delta\nu_w(T, c)p'_{\lambda\gamma}(c)(T - T_0(c)) \quad (29)$$

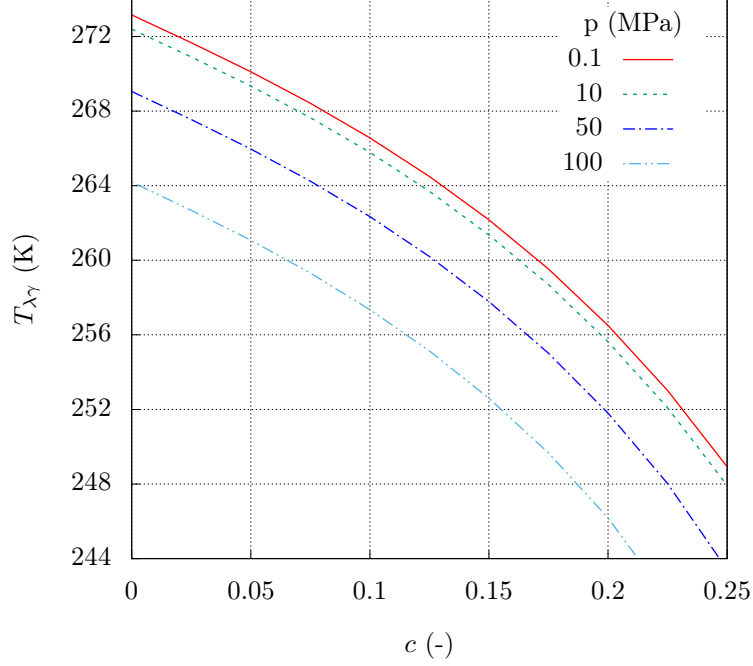


Figure 1: Representative curves of the function $T_{\lambda\gamma}(p, c)$ for four values of p .

Regarding the phase change enthalpy, two assumptions are often introduced to simplify its mathematical formulation, namely, a first order approximation for $L_{\lambda\gamma}$, and temperature-independent specific volumes $\nu_\lambda(p, T, c) = \nu_\lambda(p_0, T_0(c), c)$ and $\nu_\gamma(p, T) = \nu_\gamma(p_0, T_0(c))$ [30, 44]. This entails:

$$\Delta h_w(p_\lambda, p_\gamma, T, c) = L_{\lambda\gamma}(T, c) = L_0(c) + L'_0(c)(T - T_0(c)) \quad (30)$$

with $L_0(c) = T_0(c) \Delta\nu_{w0} p'_{\lambda\gamma}(c)$ and $\Delta\nu_{w0}(p_0, T_0(c), c) = \nu_\gamma(p_0, T_0(c)) - (\nu_\lambda - c\partial_c\nu_\lambda)(p_0, T_0(c), c)$.

The assumption of temperature-independent specific volumes allows to further simplify Equation 29 and leads to the following expression of capillary pressure that will be adopted in what follows:

$$p_c(p_\lambda, T, c) = \rho_\gamma(p_0, T_0(c)) \left(-\Delta\nu_{w0}(p_\lambda - p_0) + L_0(c)(T/T_0(c) - 1) \right) \quad (31)$$

To sum up, two main assumptions were used to derive the simplified expressions of capillary pressure (Equation 31) and phase change latent heat (Equation 30): a linear temperature dependence of the functions $p_{\lambda\gamma}$ and $L_{\lambda\gamma}$, and pressure and temperature independent

specific volumes of phases λ and γ . While the assumption of linearity is used solely to derive simplified expressions of p_c and Δh_w , the second assumption is expected to have implications on the balance equations by canceling the contribution of the transient terms related to the fluids compressibility and thermal dilation. Knowing that this hypothesis is often unwarranted in coupled hydro-mechanical problems, a distinction must then be drawn between the assumptions used to derive mechanical and chemical equilibrium conditions at the interface $\lambda\gamma$ and those used in balance equations. Undoubtedly, this methodology is not without consequences for the overall coherence of the formalism. However, one should not overestimate the significance of these inconsistencies, given that the capillary pressure and the latent heat functions intervene in the model as a parameter of an empirically determined function S_λ , or multiplied by an empirical term $\hat{\pi}^\gamma$, respectively. Consequently, the dependency of specific volumes of brine and ice upon temperature and pressure is maintained in the balance equations. For the sake of simplicity, they were supposed to be linearly correlated with temperature and pressure ($\chi_{T\alpha}$ and $\chi_{p\alpha}$ are constants) as follows:

$$\begin{cases} \nu_\gamma(p_\gamma, T) = \nu_{\gamma_0}(1 + \chi_{T\gamma}(T - T_0(0)) - \chi_{p\gamma}(p_\gamma - p_0)) \\ \nu_\lambda(p_\lambda, T, c) = \nu_{\lambda_0}(1 + \chi_{T\lambda}(T - T_0(0)) - \chi_{p\lambda}(p_\lambda - p_0))\tilde{\nu}_\lambda(c) \end{cases} \quad (32)$$

where $\nu_{\gamma_0} = \nu_\gamma(p_0, T_0(0))$ and $\nu_{\lambda_0} = \nu_\lambda(p_0, T_0(0), 0)$.

As for the thermal capacities $C_{p\alpha}$, only their variation with the concentration is considered. Indeed, the effect of this variation is significant in comparison with that of temperature and pressure:

$$C_{p\gamma} = C_{p\gamma}(p_0, T_0(0)), \quad C_{p\lambda} = C_{p\lambda}(p_0, T_0(c)) \quad (33)$$

The approximated expressions of $T_0(c)$, $L_0(c)$, $L'_0(c)$, $C_{p\lambda}(c)$, $C_{p\gamma}$, ν_{γ_0} , ν_{λ_0} , $\tilde{\nu}_\lambda(c)$, $\chi_{T\gamma}$, $\chi_{T\lambda}$, $\chi_{p\gamma}$ and $\chi_{p\lambda}$ are given in Table 1. They are determined through Least-Squares fitting of their full expression established on the basis of empirical expressions of the Gibbs free energy functions of ice and NaCl solution.

| | φ^0 | a_1 | a_2 | a_3 | b_1 | b_2 | b_3 |
|--------------------------------------------|---------------------------|----------|----------|----------|-------|-------|-------|
| ν_{γ_0} (m ³ /kg) | 1.090844×10^{-3} | | | | | | |
| $\chi_{T\gamma}$ (/K) | 0.15984×10^{-3} | | | | | | |
| $\chi_{p\gamma}$ (/MPa) | 0.11778×10^{-3} | | | | | | |
| $C_{p\gamma}$ (kJ/kg/K) | 2.09671 | | | | | | |
| ν_{λ_0} (m ³ /kg) | 1.000157×10^{-3} | | | | | | |
| $\chi_{T\lambda}$ (/K) | -0.67717×10^{-4} | | | | | | |
| $\chi_{p\lambda}$ (/MPa) | 0.50884×10^{-3} | | | | | | |
| $\tilde{\nu}_\lambda$ (m ³ /kg) | 1. | -0.701 | 0.247 | | 0.98 | 2.675 | |
| $C_{p\lambda}$ (kJ/kg/K) | 4.21944 | -3.224 | 3.356 | | 1.082 | 1.379 | |
| T_0 (K) | 273.1526 | -0.20822 | -1.08254 | -11.9205 | 0.992 | 2.576 | 5.53 |
| L_0 (kJ/kg) | -333.427 | -0.636 | 0.623 | -19.341 | 1.018 | 1.234 | 4.394 |
| L'_0 (kJ/kg/K) | -2.45825 | -0.4524 | 145.821 | 614412 | 0.79 | 3.56 | 10.17 |

Table 1: Simplified equations of state; $\varphi = \varphi^0(1 + \sum a_i c^{b_i})$. $p_0 = 0.1$ MPa.

3. Laboratory experiments and model validation

In this section, the THMC model is validated against freezing experiments. Since the objective is to study the mechanical effect induced by the freezing of a sodium chloride saturated porous material, no additional mechanical external stress was applied. Indeed, combining a thermal and a mechanical load would definitely not serve that purpose and would request, for better interpretation of results, an appropriate rheological model to account for irreversible strains. Three concentrations were studied to allow a discussion of the influence of the initial salt content of the saturating fluid on the temperature and strain response.

We note that these freezing tests have been designed primarily to further advance our understanding of THMC couplings. Furthermore, contrary to classical frost heave tests conceived for natural freezing problems, the presented freezing tests are more representative of artificial freezing in terms of the prescribed temperature magnitude, the quick cooling kinetics

and the uniform thermal boundary conditions.

In the following, ~~First~~, the experimental setup is ~~first~~ briefly described, then the presented approach is used to simulate those experiments and the obtained results are compared with the experimental data.

3.1. Laboratory experiments

The experimental campaign was conducted on the Anstrude limestone (France). This rock has been selected for its isotropy and homogeneity (**monomineral composition**) and, at the same time, its important porosity of 20% , **that is representative of the usual value of porosity in projects where the technique of artificial ground freezing is used. Moreover, its porous network allows a rapid and easy saturation of the specimens.** The physical and mechanical parameters of the Anstrude limestone are given in Table 2.

The freezing experiments were carried out using a temperature controlled environmental chamber, offering a temperature range from -30 °C to 130 °C and a maximum ramp rate of 1 °C/min. The samples are cylinders measuring 10 cm in height and 5 cm in diameter, and vacuum saturated, for one week before the test, with an aqueous solution of sodium chloride with a specific concentration. Two thermocouples were used to measure the temperature on the surface and at the center of the specimen, which required to drill a 1 mm hole through each specimen. Given the low magnitude of the thermal contraction strains of limestone, the strain gauges were chosen over other strain measurement methods. Two strain gauges were bonded to the surface of the specimen, a 60 mm long gauge in the vertical direction and a 120 mm long gauge in the horizontal direction, recording axial and circumferential strains respectively. We note that the use of gauges with long lengths enabled us to measure an averaged strain over a larger area. However, the temperature-induced apparent strain in strain gauges could be a significant source of error, given the important changes of temperature and the low magnitude of contraction thermal strains. In order to be able to correct it, identical (same length and gauge factor) compensating gauges were bonded to an Invar sample, of which the thermal expansion coefficient is known ($2. \times 10^{-6}$), and connected to the main gauges through a Wheatstone bridge circuit. Because

of phase change, temperatures on the surface of Invar and limestone samples don't remain equal throughout the test, that's why the temperature on the surface of the Invar was also monitored in order to make the necessary corrections. For more clarity, the exact location of the thermocouples and strain gauges is shown in Figure 2.

In order to test the capability of the model to reproduce experimental data of different scenarios of thermal loading, the water saturated specimens were subjected to two types of thermal loading paths: a multi-stage and a fixed rate temperature variation. Specimens saturated with an aqueous NaCl solution were subjected to a fixed rate temperature variation only in order to avoid any overlapping with the phase change temperature plateaus.

3.2. Numerical simulations

Despite the small size of the test specimens, measurements have shown that during phase change the distribution of temperature and strain becomes heterogeneous. Indeed, temperatures at the surface and inside the specimen become different. The same applies to the axial and circumferential strains. Consequently, a finite element analysis was performed to simulate the laboratory experiments, using the COMSOL software, where the theoretical formalism presented in Section 2 was implemented using the nonlinear coefficient form PDE formulation.

A constraint is added to the system of equations with regard to the salt concentration evolution. Indeed, it is known that in saline porous media subjected to freezing, the formation of ice induces an increase of the salt concentration in the remaining nonfrozen interstitial liquid until it reaches a solubility limit c_{sat} at which salt may precipitate. In the presented freezing tests, we noticed that the crystallization is particularly slow; tests of longer duration are required to observe salt efflorescences on the surface of the sample. The phenomenon of salt precipitation is then not considered for the simulation of these tests and the concentration c is assumed to respect the following inequality:

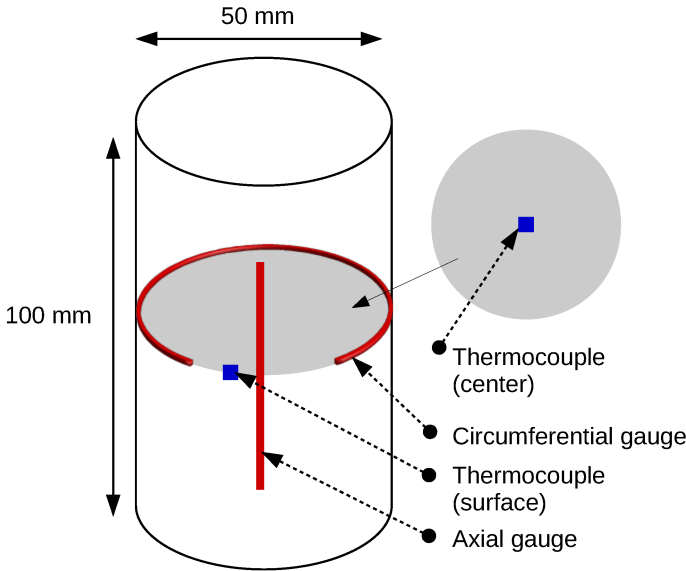
$$c \leq c_{\text{sat}}(T) \quad (34)$$

Due to the geometry and loading symmetries, only one quarter of the specimen was modeled as a 2D axisymmetric problem. The used mesh consisted of approximately 1000

eight-node quadrilateral elements. The mesh was refined to ensure the non-dependency of the results on mesh size.



(a) The specimen inside the environmental chamber.



(b) Schematic illustration of the arrangement of thermocouples and strain gauges in the specimen.

Figure 2: Testing setup.

| Parameter | | Unit | Value |
|---------------------------------------------------------------------------------------------|---------------------|------------------------------------|---------------------|
| General model parameters | \mathbf{E}_0 | GPa | 3.6 |
| | \mathbf{E}_f | GPa | 7.2 |
| | ν_0 | | 0.22 |
| | ν_f | | 0.3 |
| | ρ_σ | kg m ⁻³ | 2500 |
| | $C_{p\sigma}$ | J kg ⁻¹ K ⁻¹ | 900 |
| | \mathbf{K}_σ | GPa | 80 |
| | n | | 0.2 |
| | D_λ | m ² s ⁻¹ | 10 ⁻¹⁴ |
| | Equation 35 | m | |
| P | | MPa | 0.3 |
| Equations 36 and 37 | k_0 | m ² | 9×10 ⁻¹⁶ |
| | r | | 0.9 |
| Equation 38 | (a_1, a_2, a_3) | | (1.85, 4.1, 44.5) |
| | (b_1, b_2, b_3) | | (1, 2, 3) |
| Equation 39 | Λ_λ | W m ⁻¹ K ⁻¹ | 0.6 |
| | Λ_γ | W m ⁻¹ K ⁻¹ | 2.3 |
| | Λ_σ | W m ⁻¹ K ⁻¹ | 2 |
| Equation 40 | H | W m ⁻² K ⁻¹ | 20 |
| $c_{\text{sat}}(T) = 0.2626 + 0.535 \theta^{1.888} - 0.479 \theta^2, \theta = T/T_0(0) - 1$ | | | |
| $\eta_0(T) = 1.034 \times 10^{-4} (\theta + 0.1616)^{-1.562}$ | | | |
| $\mathbf{A}(T) = (3.7735 + 8.4731 \theta + 9.6996 \theta^2) 10^{-6}$ | | | |

Table 2: Constants for numerical simulations.

3.2.1. Parameters calibration

The previously mentioned coefficients, namely S_λ , k_λ , η_λ , Λ , D_λ and \mathbf{A} are either experimentally determined or estimated through empirical models that are commonly used in

literature. This paragraph details the approach used to identify each parameter.

First, in order to express the liquid saturation degree S_λ , the van Genuchten empirical function [41] was chosen for its widespread applicability in ground freezing studies, especially when the porous medium is initially saturated with pure water [7, 26, 51]. In addition, it was recently successfully extrapolated to porous media where the saturating fluid is an aqueous solution [30]. Its expression can be written as follows:

$$S_\lambda(p_c) = \left(1 + (p_c/P)^{1/(1-m)}\right)^{-m} \quad (35)$$

which involves two material parameters, m and P .

With regard to the permeability for liquid phase flow k_λ , it is usually defined as a product of an intrinsic permeability k_0 (m^2), characteristic of the structure of the porous space regardless of the flowing phases, and a liquid relative permeability k_r function only of the liquid saturation degree, to account for the effect of ice presence on reducing the liquid phase flow:

$$k_\lambda = k_0 k_r(S_\lambda) \quad (36)$$

The intrinsic permeability being already identified in previous works, the unknown is therefore the relative permeability function which expression is classically [26, 31] derived from the van Genuchten model [25] and introduces one additional material parameter r , as follows:

$$k_r(S_\lambda) = \sqrt{S_\lambda} \left(1 - (1 - S_\lambda^{1/r})^r\right)^2 \quad (37)$$

The liquid phase viscosity is a function of pressure, temperature and concentration, as follows:

$$\eta_\lambda = \eta_0(T, p_\lambda) \left(1 + \sum a_i c^{b_i}\right) \quad (38)$$

where η_0 is the dynamic viscosity of pure water (Pa s). Its variation with pressure can be neglected compared to the variation caused by temperature, especially in the pressure and temperature ranges that are considered in this paper [27]. The influence of temperature is described using a power law given by Gawin et al. [15]. The parameters a_i and b_i used in

this equation, to account for the salinity dependence, are those given by Koniarczyk and Gawin [20].

The thermal conductivity of the porous media Λ is recurrently expressed by a geometric mean of the thermal conductivities of the phases [5, 26, 30]:

$$\Lambda = \Lambda_{\sigma}^{n_{\sigma}} \Lambda_{\lambda}^{n_{\lambda}} \Lambda_{\gamma}^{n_{\gamma}} = \Lambda_{\sigma}^{1-n} \Lambda_{\lambda}^{n S_{\lambda}} \Lambda_{\gamma}^{n(1-S_{\lambda})} \quad (39)$$

where Λ_{σ} , Λ_{λ} and Λ_{γ} , the conductivities of the three phases, are assumed to remain constant in the present work.

The diffusivity coefficient D_{λ} , generally dependent on many factors (porous medium, type of solute-solvent, temperature. . .), is assumed constant.

Concerning the thermal expansion coefficient \mathbf{A} , it was deduced from a stress-free cooling test on a dried limestone. Figure 3 shows the thermal contraction of a dried limestone $\mathbf{A}\Delta T$ and the fitted curve from which the thermal expansion coefficient was determined.

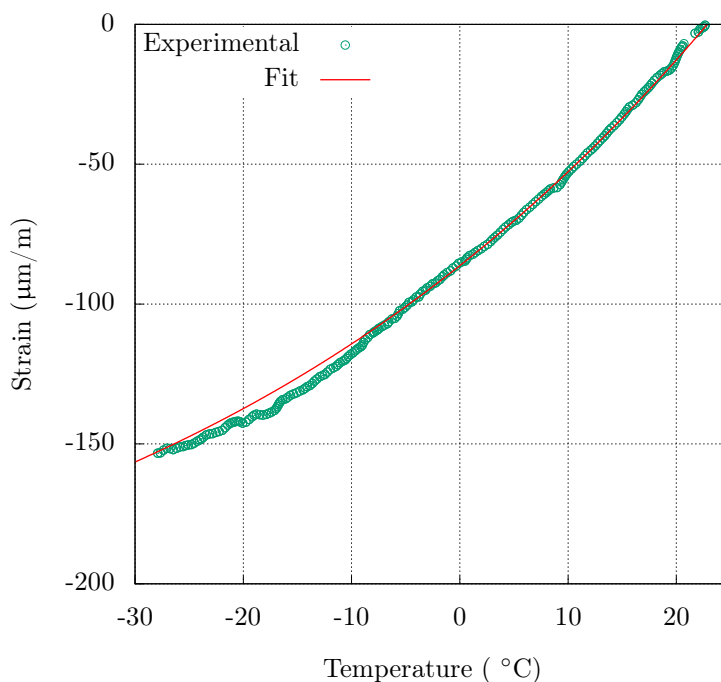


Figure 3: Thermal strain of a dried limestone specimen.

The parameters used in all the numerical simulations are listed in Table 2. Notice that the parameters of the water saturation degree (m and P) and the relative permeability (r)

were calibrated against freezing tests with pure water and multi-stage loading conditions. An example of fitting a stress-free multi-stage freezing laboratory test performed on a water saturated specimen is shown in Figures 4 and 5. As can be observed, the calibrated values of the parameters m , P and r allowed to satisfactorily describe the evolution of temperature and strain in the specimen.

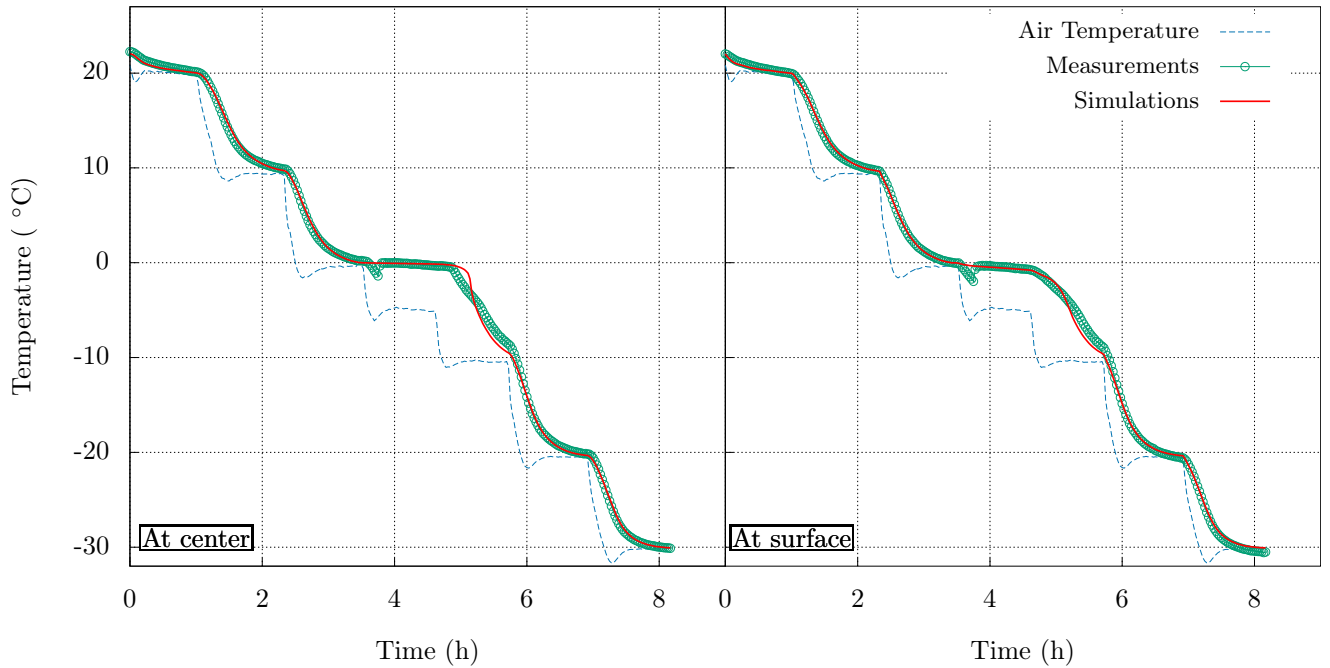


Figure 4: Comparison between measured and predicted temperatures for $c = 0$, in the case of a multi-stage temperature variation.

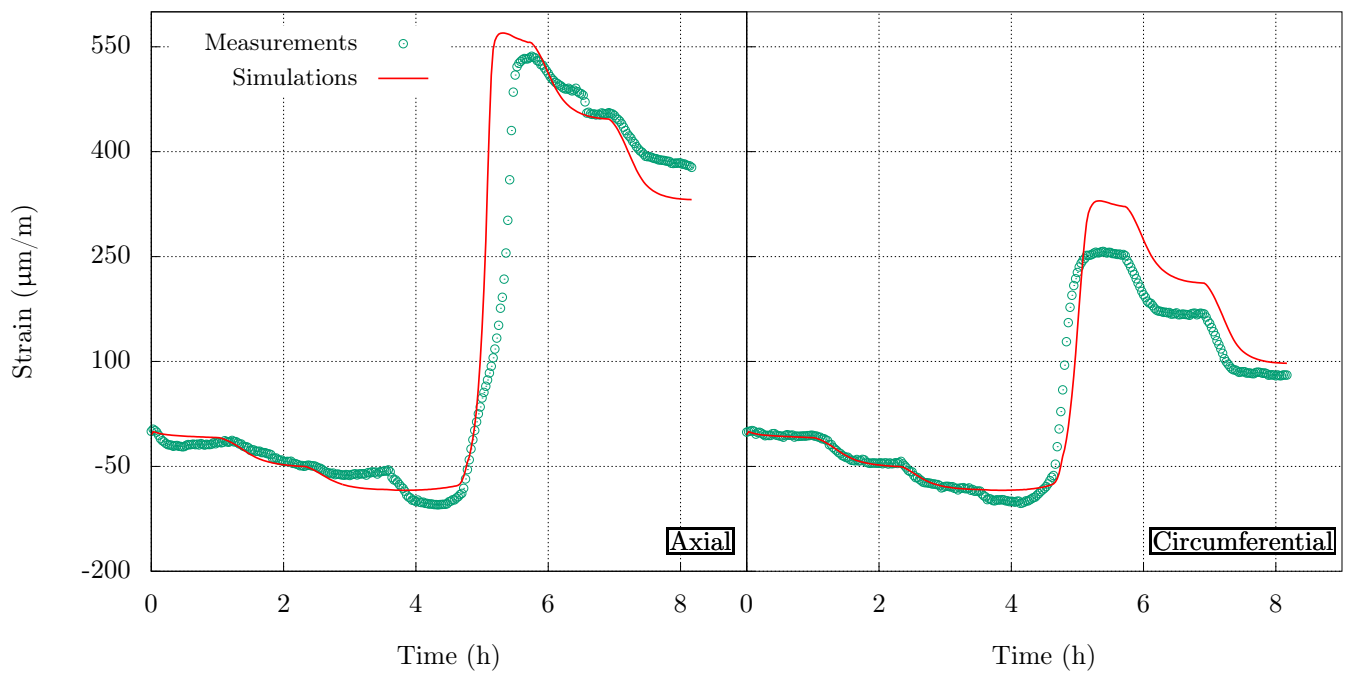


Figure 5: Comparison between measured and predicted strains for $c = 0$, in the case of a multi-stage temperature variation.

3.2.2. Initial and boundary conditions

Temperature and concentration were initially set to their respective values at the beginning of each experimental test, and the liquid pressure was initially equal to p_0 .

The thermal boundary conditions were simulated using the Newton's law of cooling, as follows:

$$\vec{\psi} \cdot \vec{n} = H (T - T_a) \quad (40)$$

where H is the convective heat transfer coefficient, T_a is the air temperature inside the environmental chamber and \vec{n} is the outward unit vector normal to the boundary of the sample.

A zero-flux boundary condition was imposed for concentration (in the case of NaCl saturated specimens) and a free drainage boundary condition for liquid phase pressure:

$$\begin{cases} \vec{J} \cdot \vec{n} = 0 \\ p_\lambda = p_0 \end{cases} \quad (41)$$

3.2.3. Numerical results and comparison with experimental data

In this section we compare the numerical predictions, in terms of temperature and mechanical strain, with experimental results of three stress-free freezing tests corresponding to three different concentrations. For each test, two figures are presented: a figure depicting the variation of temperature versus time inside the specimen and on its surface in addition to the air temperature T_a recorded inside the environmental chamber, and a figure showing the variation in time of axial and circumferential strains. In both figures, experimental values and calculated curves are given. Figures 6 and 7 correspond to the case of a water saturated specimen whereas Figures (8, 9) and (10, 11) show the results of aqueous solution saturated specimens, corresponding to an initial concentration equal to 0.08 and 0.14, respectively. As can be seen, the numerical results (solid lines) agree fairly well with the experimental data (circle points) for the three salinity levels. Moreover, several observations can be drawn from these figures.

First, it can be observed that, contrary to the temperature curves of the water saturated specimen showing only one phase change plateau around 0 °C (Figures 4 and 6), the

temperature curves for the concentrations 0.08 and 0.14 exhibit two phase change plateaus (Figures 8 and 10): the first one around the phase change temperature corresponding to the initial salinity of the specimen's saturating fluid ($-5\text{ }^{\circ}\text{C}$ for $c = 0.08$ and $-10\text{ }^{\circ}\text{C}$ for $c = 0.14$) and the other one around the phase change temperature of a saturated NaCl aqueous solution ($-25\text{ }^{\circ}\text{C}$ for $c = 0.25$, approximately). It should be noted that this second plateau is due to the constraint we added on the concentration variable so that it does not exceed the saturation level. Figure 12 illustrates this phenomenon, showing the evolution of salt concentration inside the specimen in its center versus temperature for the two salinities. Remark also that the phase change plateaus are less pronounced than in the case of pure water, especially the first one, which may be explained by the evolution rate of salt concentration in the saturating liquid and the resulting decrease of the coexistence temperature.

Second, as can be seen in all the temperature curves, when the specimen's temperature reaches the phase change temperature, it decreases instead of remaining constant and phase change does not occur. It is an unstable condition, called supercooling, and followed by a nucleation phase during which temperature instantly increases up to the phase change temperature. The phenomenon of supercooling, still difficult to predict, is not considered in this work.

SecondThird, the strain curves in the case of pure water (Figures 5 and 7) exhibit three major characteristic phases, a first phase during which the specimen only contracts, corresponding in the temperature curve to the first decay of temperature beyond the freezing-melting temperature (around $0\text{ }^{\circ}\text{C}$), a second phase when phase change occurs inducing an important dilation in the axial and circumferential directions, and a third phase in which transformation of water into ice ceases and the specimen restarts contracting but following a slope larger than the slope of the first phase due to the presence of the newly formed ice phase. The same thing applies to the strain curves for the concentrations 0.08 and 0.14 (Figures 9 and 11). Indeed, the initial pure contraction of the specimen ends at the shifted freezing-melting temperature corresponding to the first change of temperature rate then the specimen continues to contract following a less steep slope since ice crystals start to

form. This change in strain rate remains negligible in front of the dilation that occurs when the saturation concentration is reached, partly due to the important length of the second plateau compared to the first one. We notice here that the model is capable of reproducing this significant strain increase accompanying the saturation plateau but underestimates the dilation occurring after the first freezing plateau. However, the overall strain magnitude remains close to the measured values. Naturally, the quality of the numerical curve could be enhanced if the saturation degree and relative permeability parameters were determined independently for each specimen instead of using one global parameter set to simulate all the tests.

The prevailing mechanism behind the swelling of specimens upon freezing is the mass density discontinuity associated with water phase change. This induces a significant increase of the equivalent pore pressure ϖ (Equation 20) as the temperature of the specimen decreases below the freezing-melting temperature. Figure 13 depicts the evolution of the equivalent pore pressure inside the specimens. Notice that for the concentrations 0.08 and 0.14, this increase, in full accordance with axial and circumferential dilations, becomes significant when temperature reaches the freezing-melting point of the saturated solution. We note also that the greater the initial salt content, the more important the strain and pore pressure magnitude. This can be partly explained by the increase of the liquid dynamic viscosity with an increasing salinity (Equation 38) which induces a decrease of the permeability resulting in a very high liquid pressurization during freezing. In practice, it is important to note that freezing induces a rapid growth of the remaining liquid water's concentration (Figure 12) which could affect the magnitude of ground deformations and the conclusions drawn about the stability of the medium, despite a low initial salt content of the saturating fluid.

Third**Fourth**, we noticed that the maximum recorded circumferential strain was smaller than the axial strain at a ratio of about 0.7, except in the case of $c = 0.08$, where circumferential strains exceeded axial strains. Indeed, a material variability is suspected to influence the tendency. Simulations showed that temperature evolution during freezing is responsible for the observed differences between the axial and circumferential strains. To illustrate this, Figure 14 depicts temperature and pressure distribution and the corresponding deformed

shape of the specimen at three key dates in the case of $c = 0.14$. The displacement scaling factor is not the same for the three dates due to the large difference between the magnitude of contraction and dilation strains. It appears that the borders of the top and the bottom bases (by symmetry) of the cylindrical specimen always reveal high negative temperature values compared to the center. A quicker cooling of that part of the specimen modifies the direction of the temperature gradient and induces a heterogeneous growth of the equivalent pore pressure ϖ when water starts turning into ice. Indeed, in the first phase, when the specimen contracts (Figure 14a), the pore pressure remains nearly equal to the initial pressure given the drained conditions. Consequently, the resulting strain distribution is quite homogeneous. Then, water in the borders of the specimen start first to turn into ice (Figure 14b), and as a consequence, pore pressure increases in the corners inducing a heterogeneous expansion of the specimen that becomes hourglass-shaped. As the freezing front advanced in the other lateral zones of the specimen and towards the center (Figure 14c), the pore pressure and the magnitude of volumetric expansion increase inside the specimen that becomes barrel-shaped.

We should emphasize here the importance of carefully choosing the right boundary conditions that allow to reproduce empirical observations. In our case, if a Dirichlet boundary condition was applied instead of the Newton's law (Equation 40), we wouldn't be able to explain the noted difference between axial and circumferential strains.

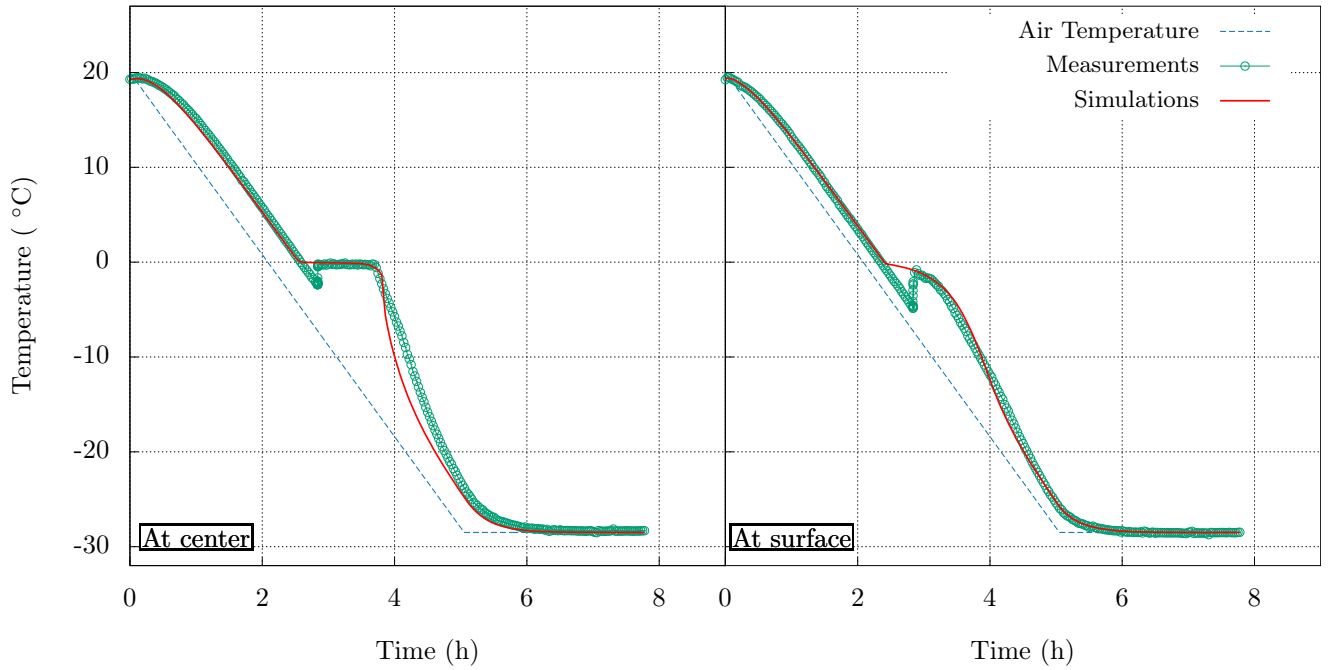


Figure 6: Comparison between measured and predicted temperatures for $c = 0$, in the case of a fixed rate temperature variation.

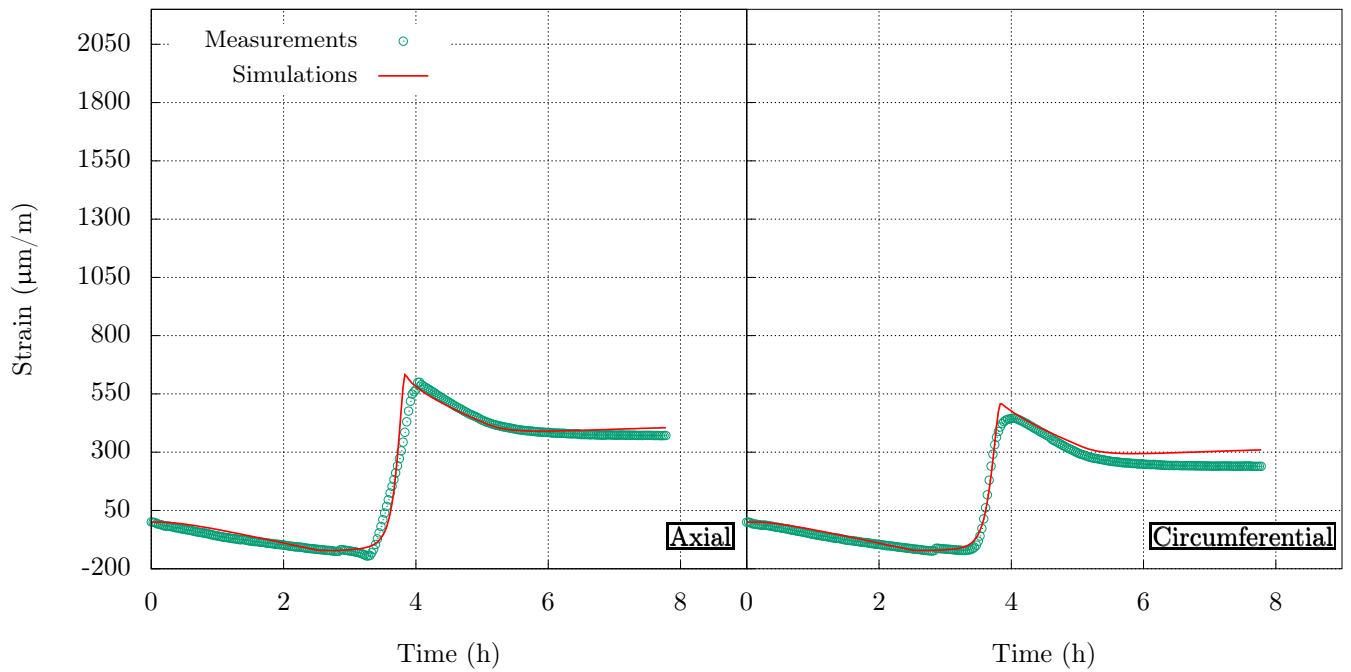


Figure 7: Comparison between measured and predicted strains for $c = 0$, in the case of a fixed rate temperature variation.

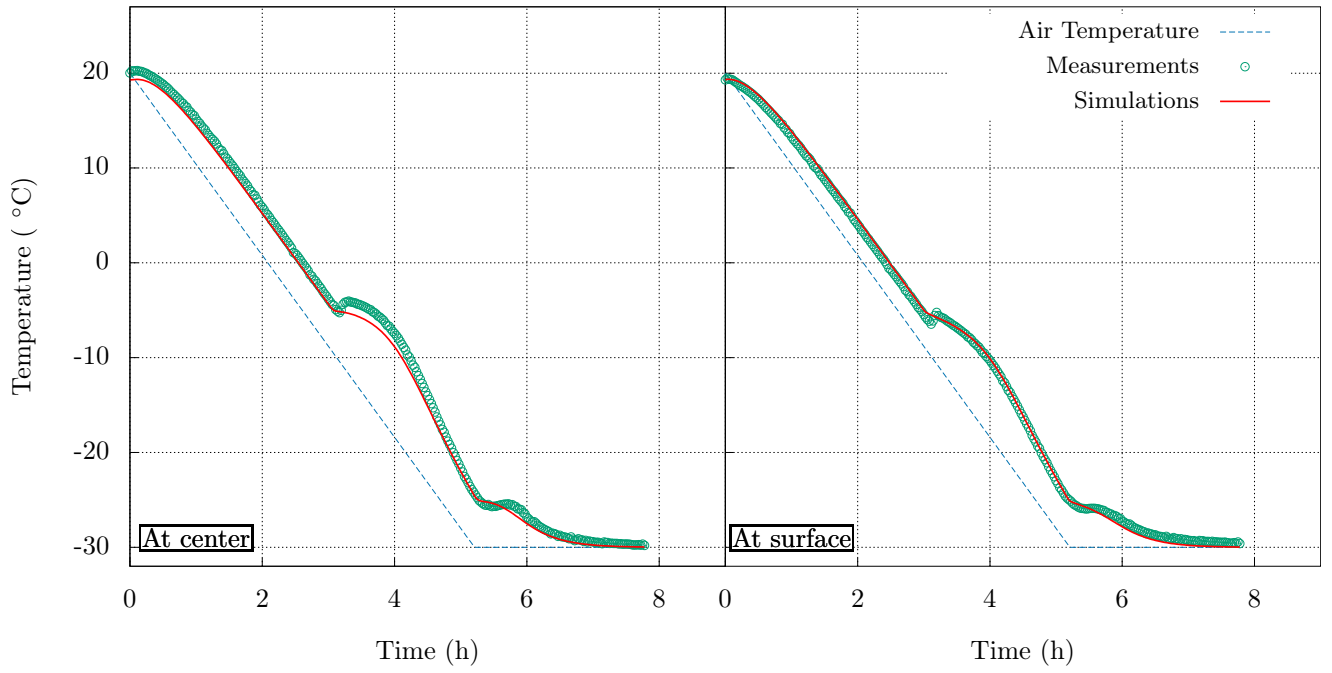


Figure 8: Comparison between measured and predicted temperatures for $c = 0.08$.

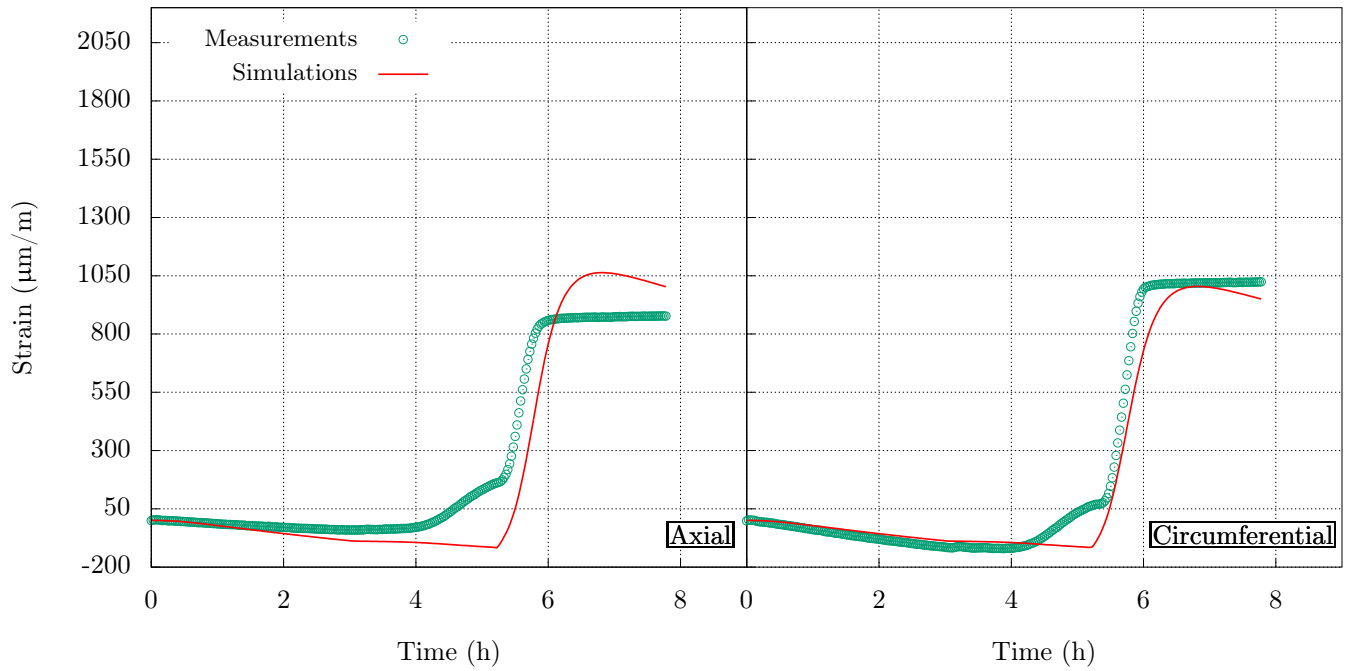


Figure 9: Comparison between measured and predicted strains for $c = 0.08$.

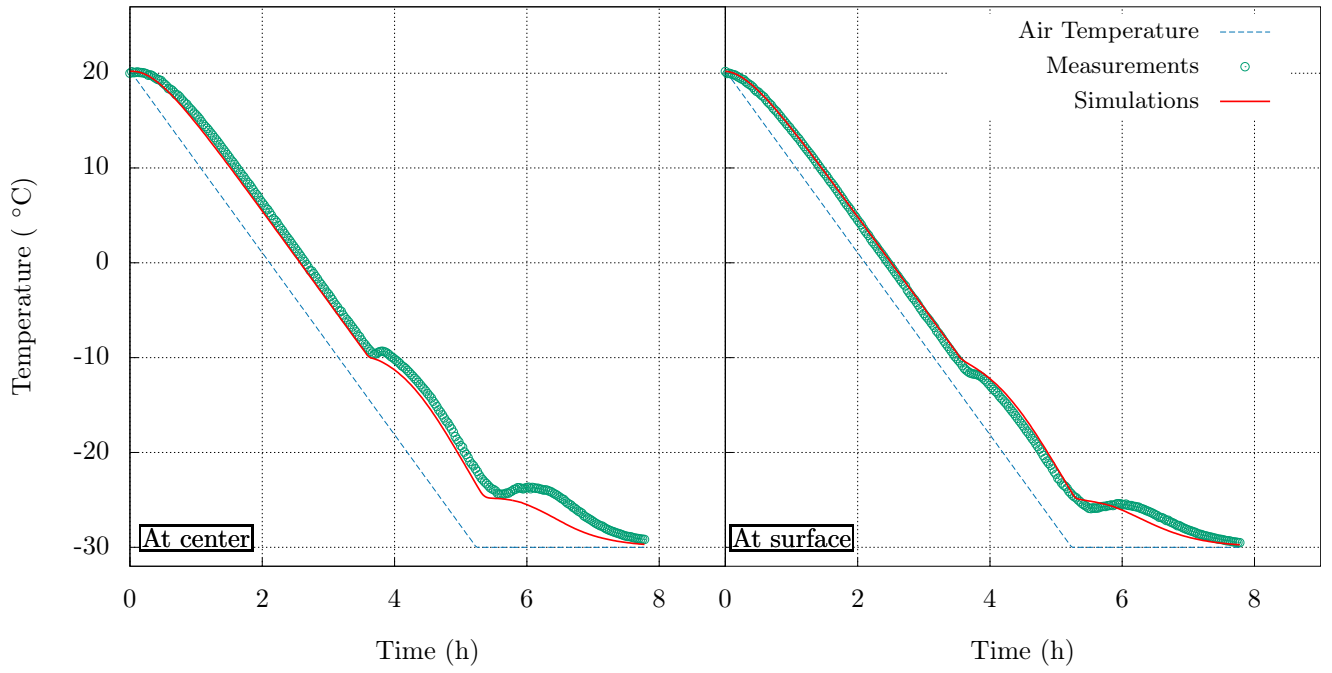


Figure 10: Comparison between measured and predicted temperatures for $c = 0.14$.

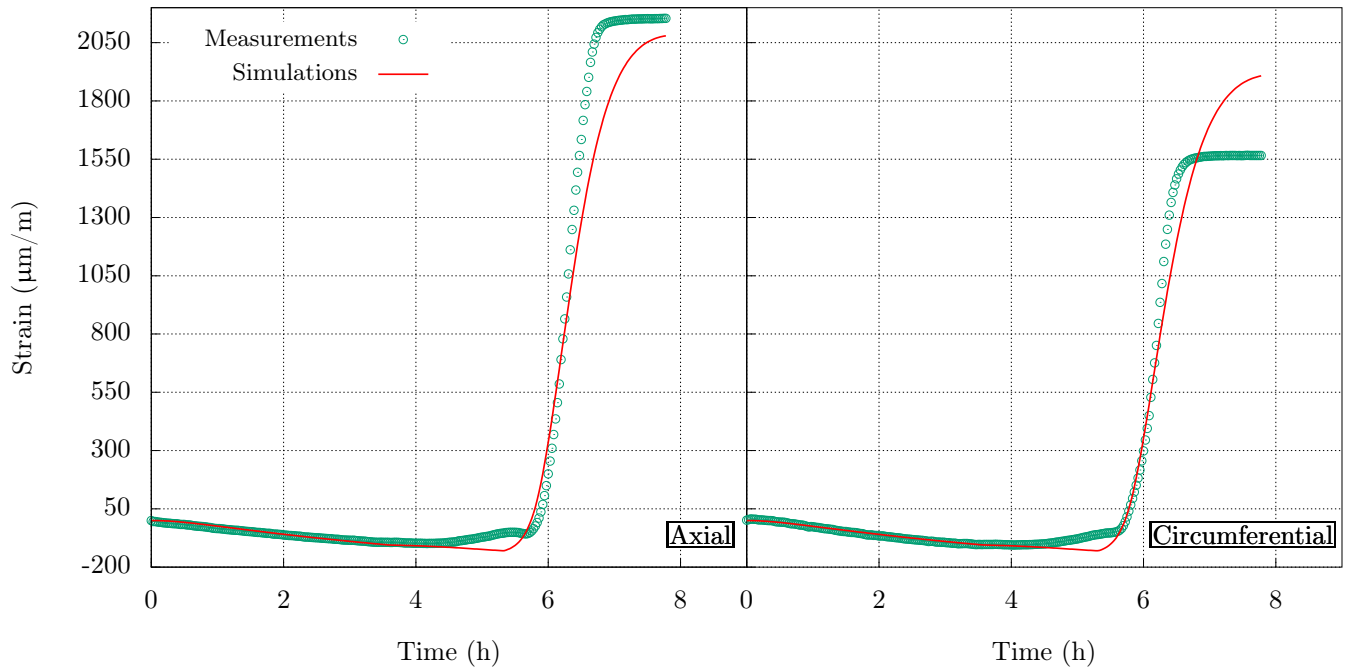


Figure 11: Comparison between measured and predicted strains for $c = 0.14$.

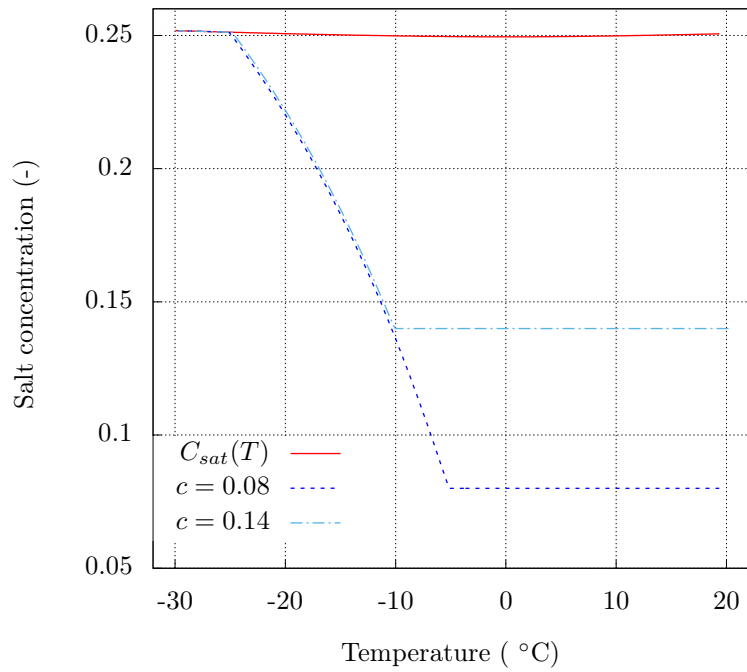


Figure 12: Evolution of concentration inside the specimen for $c = 0.08$ and $c = 0.14$.

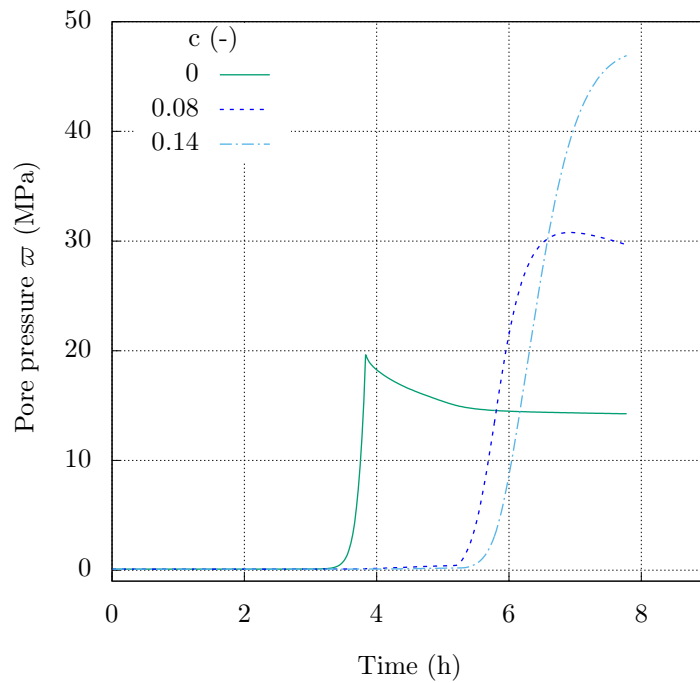
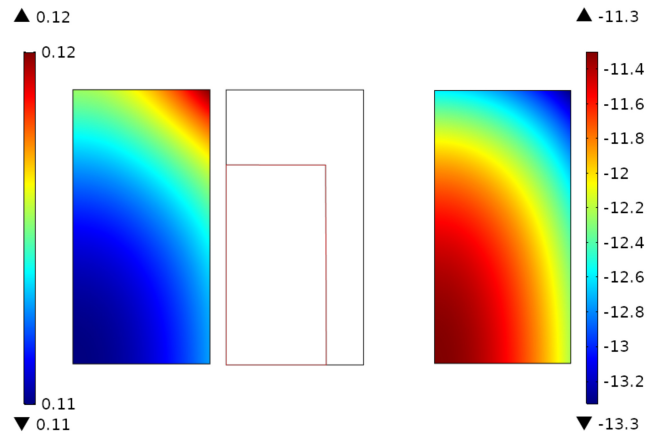
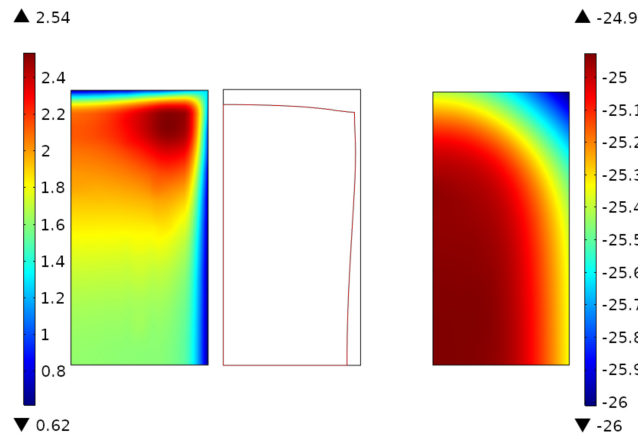


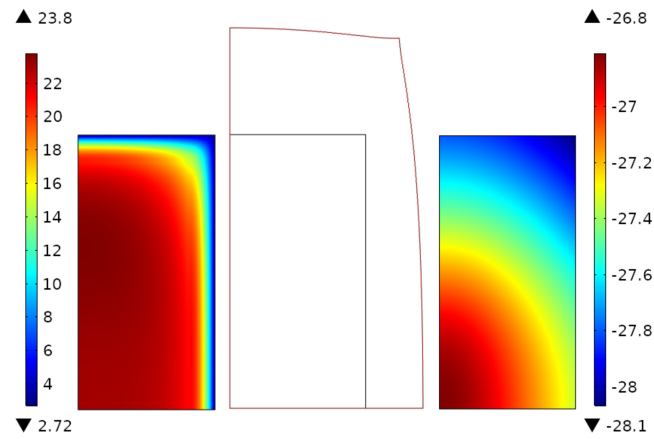
Figure 13: Evolution of the equivalent pore pressure ϖ inside the specimen for $c = 0$, $c = 0.08$ and $c = 0.14$.



(a) $t = 4$ h



(b) $t = 5.7$ h



(c) $t = 6.4$ h

Figure 14: Equivalent pore pressure in MPa (on the left) and temperature in $^{\circ}\text{C}$ (on the right) distribution, and specimen's deformed shape (in the center), with a displacement scaling factor of 2500 in (a) and (b) and 400 in (c), for $c = 0.14$.

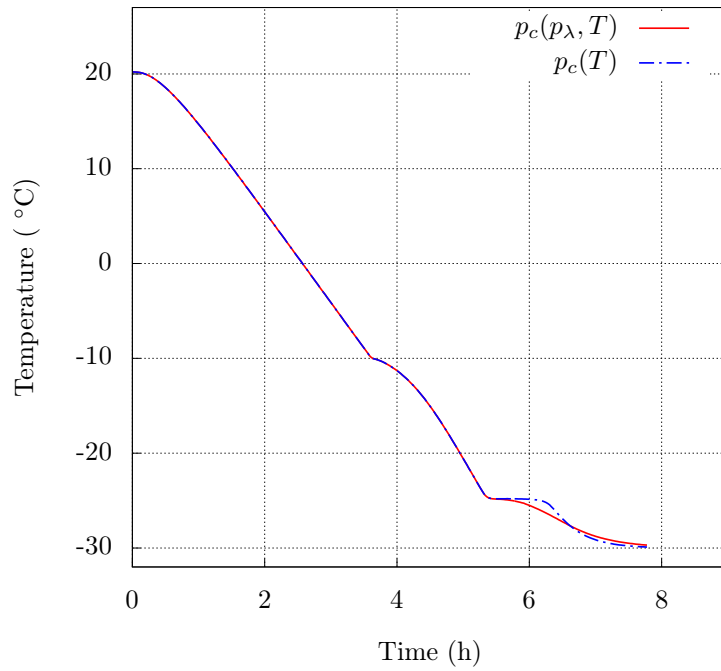
3.2.4. Effect of neglecting the liquid pressure contribution in the capillary pressure

In order to demonstrate this effect, a simulation of the test with $c = 0.14$, in which this contribution was neglected, was performed for comparison purposes. This assumption is equivalent to considering the following expression of capillary pressure:

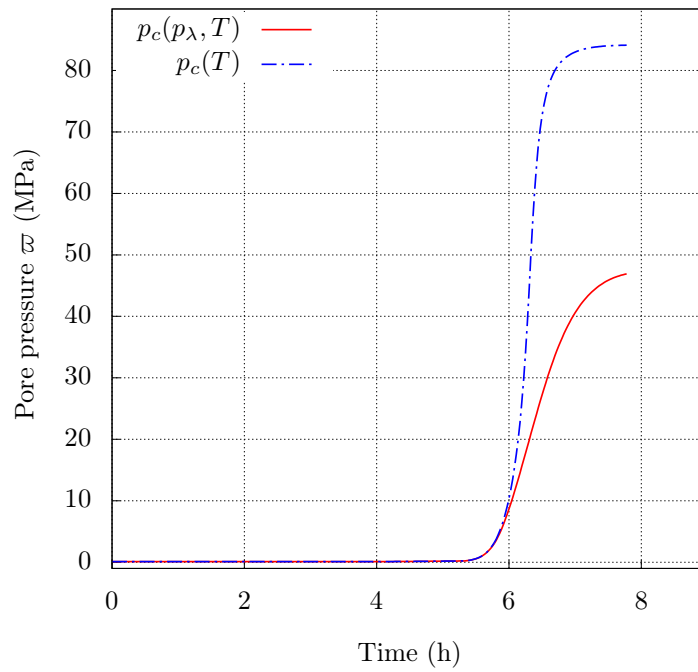
$$p_c(T, c) = \rho_\gamma(p_0, T_0(c))L_0(c)(T/T_0(c) - 1) \quad (42)$$

This equation is classically adopted in literature on thermo-hydraulic modeling of ground freezing [30, 44]. The resulting mathematical formulation is obviously more simple than the one used in this paper but remains consistent with the level of approximation involved in large-scale geotechnical applications, in particular when the main issue is the prediction of the extent of the frozen area. When the problem is about the prediction of the freezing-induced ground deformations, the influence of such assumption could be detrimental to the model's predictive capacities, especially in the presence of undrained ground conditions that are favorable to a strong growth of liquid pressure beyond the initial pressure upon freezing. Literature about free-dilation sealed experiments on mortar specimens [9] showed that neglecting the effect of liquid pressurization in the capillary pressure expression induces an overestimation of the amount of the ice formed and therefore an overestimation of the pressure of the remaining unfrozen water.

In Figure 15, we compare temperature (Figure 15a) and equivalent pore-pressure (Figure 15b) in the center of the specimen in both cases: when using Equation 31 to express capillary pressure and when using the simplified expression 42. As can be observed, while the difference in terms of the calculated temperatures remains small, it is very significant in terms of the calculated pore pressures: when using Equation 42 the pore pressure is largely overestimated. The deformations being mainly pore-pressure controlled, the impact on them is therefore non-negligible.



(a)



(b)

Figure 15: Comparison between simulated temperature and pore pressure in the center of the specimen when using Equation 31 or Equation 42.

4. Conclusion

Through a thermodynamically consistent framework, a fully coupled THM model considering the salinity of the saturating fluid has been derived. It was built using a macroscopic continuum approach based on the liquid saturation degree function to track the phase-change fronts and on the concept of effective stress to predict the mechanical effect of ground freezing. The expressions of the capillary pressure and the latent heat of phase change as functions of liquid pressure, temperature and concentration were derived based on the thermodynamic equilibrium at the liquid-ice phases interfaces and some simplifying assumptions. The independence of the specific volumes with respect to T and p is the most questionable one among these assumptions as it was not integrated in balance equations, to the detriment of the model's global consistency. However, this inconsistency remains minor given that the capillary pressure and the latent heat terms intervene in the model as a parameter of an empirical function, or multiplied by an empirical expression, respectively.

The developed approach was used to simulate stress-free freezing laboratory tests carried out on specimens initially fully saturated with sodium chloride solutions at three different concentrations. The numerical predictions seemed to be in good agreement with the experimental measurements of both temperature and strain. In addition, it was found that the expansion of water when turning into ice leads to the build up of significant pore pressure, which represents the leading mechanism behind specimen's volumetric dilation. Moreover, this dilation is more important in the presence of salt in the saturating fluid. Consequently, if the effect of the salt concentration is ignored or not correctly modeled, the evolution of the frozen zones and the ground's movements can be mispredicted.

Although the model's ability to capture the main thermo-hydro-mechanical phenomena associated with the freezing of saline-saturated porous media was satisfactory, further investigation would be required to improve the proposed modeling approach and increase its predictive capabilities. First, further studies are required to investigate the validity of the use of the van Genuchten empirical model for the liquid saturation degree and the relative permeability functions for saline-saturated ground. Second, future work can focus on salt

crystallization phenomenon and its effect on the freezing advance and the ground's deformation. Additional freezing tests could be undertaken with a high initial salt content close to the saturation concentration and with a longer duration in order to enable the crystallization. **Finally Third**, an investigation of the thawing phase and the volume shrinkage caused by ice melting is also of great interest to geotechnical applications of ground freezing. **Finally, in the case when loading/unloading mechanisms are taking place in a frozen ground, the modeling framework presented in this paper must be supplemented with an appropriate constitutive model that is able to predict non-elastic strains.**

Acknowledgements

The authors acknowledge their collaborators from Orano for their contribution to this work, performed as part of a PhD project.

References

- [1] Archer, D. G., Carter, R. W., 2000. Thermodynamic properties of the nacl+ h₂o system. 4. heat capacities of h₂o and nacl (aq) in cold-stable and supercooled states. *The Journal of Physical Chemistry B* 104 (35), 8563–8584.
- [2] Bing, H., Ma, W., 2011. Laboratory investigation of the freezing point of saline soil. *Cold Regions Science and Technology* 67 (1-2), 79–88.
- [3] Bittelli, M., Flury, M., Roth, K., 2004. Use of dielectric spectroscopy to estimate ice content in frozen porous media. *Water resources research* 40 (4).
- [4] Black, P. B., Tice, A. R., 1989. Comparison of soil freezing curve and soil water curve data for windsor sandy loam. *Water Resources Research* 25 (10), 2205–2210.
- [5] Côté, J., Konrad, J.-M., 2005. A generalized thermal conductivity model for soils and construction materials. *Canadian Geotechnical Journal* 42 (2), 443–458.
- [6] Coussy, O., 1991. *Mécanique des milieux poreux*. Editions Technip.
- [7] Coussy, O., 2005. Poromechanics of freezing materials. *Journal of the Mechanics and Physics of Solids* 53 (8), 1689–1718.
- [8] Coussy, O., Monteiro, P. J., 2008. Poroelastic model for concrete exposed to freezing temperatures. *Cement and Concrete Research* 38 (1), 40–48.
- [9] Coussy, O., Monteiro, P. J., 2009. Errata to “poroelastic model for concrete exposed to freezing temperatures” [cement and concrete research 38 (2008) 40–48]. *Cement and Concrete Research* 39 (4), 371.

- [10] Crippa, C., Manassero, V., 2006. Artificial ground freezing at sophiaspoortunnel (the netherlands)—freezing parameters: Data acquisition and processing. In: *GeoCongress 2006: Geotechnical Engineering in the Information Technology Age*. pp. 1–6.
- [11] Fabbri, A., 2006. Physico-mécanique des matériaux cimentaires soumis au gel-dégel. Ph.D. thesis, Université de Marne la Vallée.
- [12] Fabbri, A., Fen-Chong, T., 2013. Indirect measurement of the ice content curve of partially frozen cement based materials. *Cold Regions Science and Technology* 90, 14–21.
- [13] Feistel, R., Wagner, W., 2006. A new equation of state for h₂o ice ih. *Journal of Physical and Chemical Reference Data* 35 (2), 1021–1047.
- [14] Fer, F., 1971. Thermodynamique macroscopique. 2. Vol. 2. ME Sharpe.
- [15] Gawin, D., Majorana, C., Schrefler, B., 1999. Numerical analysis of hygro-thermal behaviour and damage of concrete at high temperature. *Mechanics of Cohesive-frictional Materials: An International Journal on Experiments, Modelling and Computation of Materials and Structures* 4 (1), 37–74.
- [16] Ghoreishian Amiri, S., Grimstad, G., Kadivar, M., Nordal, S., 2016. Constitutive model for rate-independent behavior of saturated frozen soils. *Canadian Geotechnical Journal* 53 (10), 1646–1657.
- [17] Hassanizadeh, S. M., Gray, W. G., 1990. Mechanics and thermodynamics of multiphase flow in porous media including interphase boundaries. *Advances in water resources* 13 (4), 169–186.
- [18] Hu, J., Liu, Y., Li, Y., Yao, K., 2018. Artificial ground freezing in tunnelling through aquifer soil layers: a case study in nanjing metro line 2. *KSCE Journal of Civil Engineering*, 1–7.
- [19] Hu, X., Fang, T., Chen, J., Ren, H., Guo, W., 2018. A large-scale physical model test on frozen status in freeze-sealing pipe roof method for tunnel construction. *Tunnelling and Underground Space Technology* 72, 55–63.
- [20] Koniorczyk, M., Gawin, D., 2008. Heat and moisture transport in porous building materials containing salt. *Journal of Building Physics* 31 (4), 279–300.
- [21] Koopmans, R. W. R., Miller, R., 1966. Soil freezing and soil water characteristic curves. *Soil Science Society of America Journal* 30 (6), 680–685.
- [22] Lai, Y., Pei, W., Zhang, M., Zhou, J., 2014. Study on theory model of hydro-thermal-mechanical interaction process in saturated freezing silty soil. *International Journal of Heat and Mass Transfer* 78, 805–819.
- [23] Lai, Y., Wu, D., Zhang, M., 2017. Crystallization deformation of a saline soil during freezing and thawing processes. *Applied Thermal Engineering* 120, 463–473.
- [24] Mandolini, A., Viggiani, G. M., 2017. Experiences gathered from the construction of napoli underground. *Procedia Engineering* 172, 31–41.
- [25] Mualem, Y., 1978. Hydraulic conductivity of unsaturated porous media: generalized macroscopic ap-

- proach. *Water Resources Research* 14 (2), 325–334.
- [26] Nishimura, S., Gens, A., Olivella, S., Jardine, R., 2008. Thm-coupled finite element analysis of frozen soil: formulation and application. *Géotechnique* 59 (3), 159–171.
- [27] Ophori, D. U., 1998. Flow of groundwater with variable density and viscosity, atikokan research area, canada. *Hydrogeology Journal* 6 (2), 193–203.
- [28] Pimentel, E., Sres, A., Anagnostou, G., 2012. Large-scale laboratory tests on artificial ground freezing under seepage-flow conditions. *Geotechnique* 62 (3), 227.
- [29] Qinguo, M., Yuanming, L., Mingyi, Z., 2017. Freezing-thawing behaviour of saline soil with various anti-saline measures. *European Journal of Environmental and Civil Engineering*, 1–25.
- [30] Rouabhi, A., Jahangir, E., Tounsi, H., 2018. Modeling heat and mass transfer during ground freezing taking into account the salinity of the saturating fluid. *International Journal of Heat and Mass Transfer* 120, 523–533.
- [31] Rouabhi, A., Tijani, M., 2017. Modélisation thermo-hydraulique de la congélation artificielle des terrains avec prise en compte de la salinité de l'eau. In: Gasc-Barbier, M., Merrien-Soukatchoff, V., Berest, P. (Eds.), *Manuel de mécanique des roches. Thermomécanique des roches. Tome V. Presses des Mines, Collection sciences de la terre et de l'environnement*, Paris, pp. 305–316.
- [32] Russo, G., Corbo, A., Cavuoto, F., Autuori, S., 2015. Artificial ground freezing to excavate a tunnel in sandy soil. measurements and back analysis. *Tunnelling and Underground Space Technology* 50, 226–238.
- [33] Schmall, P., Dawson, A., 2017. Ground-freezing experience on the east side access northern boulevard crossing, new york. *Proceedings of the Institution of Civil Engineers-Ground Improvement* 170 (3), 159–172.
- [34] Schmall, P. C., Maishman, D., 2007. Ground freezing a proven technology in mine shaft sinking. *Tunnels and Underground Construction Magazine* 59 (6), 25–30.
- [35] Shen, C., McKinzie, B., Arbabi, S., et al., 2010. A reservoir simulation model for ground freezing process. In: *SPE Annual Technical Conference and Exhibition*. Society of Petroleum Engineers.
- [36] Spaans, E. J., Baker, J. M., 1996. The soil freezing characteristic: Its measurement and similarity to the soil moisture characteristic. *Soil Science Society of America Journal* 60 (1), 13–19.
- [37] Taber, S., 1930. The mechanics of frost heaving. *The Journal of Geology* 38 (4), 303–317.
- [38] Thomas, H. R., Cleall, P. J., Li, Y., Harris, C., Kern-Luetschg, M., 2009. Modelling of cryogenic processes in permafrost and seasonally frozen soils. *Geotechnique* 59 (3), 173–184.
- [39] Tian, H., Wei, C., Wei, H., Zhou, J., 2014. Freezing and thawing characteristics of frozen soils: Bound water content and hysteresis phenomenon. *Cold Regions Science and Technology* 103, 74–81.
- [40] Tounsi, H., Rouabhi, A., Tijani, M., Guérin, F., 2019. Thermo-hydro-mechanical modeling of artificial

- ground freezing: Application in mining engineering. *Rock Mechanics and Rock Engineering*, 1–19.
- [41] Van Genuchten, M. T., 1980. A closed-form equation for predicting the hydraulic conductivity of unsaturated soils. *Soil science society of America journal* 44 (5), 892–898.
- [42] Vitel, M., 2015. Modélisation thermo-hydraulique de la congélation artificielle des terrains. Ph.D. thesis, Paris, ENMP.
- [43] Vitel, M., Rouabhi, A., Tijani, M., Guérin, F., 2015. Modeling heat transfer between a freeze pipe and the surrounding ground during artificial ground freezing activities. *Computers and Geotechnics* 63, 99–111.
- [44] Vitel, M., Rouabhi, A., Tijani, M., Guérin, F., 2016. Modeling heat and mass transfer during ground freezing subjected to high seepage velocities. *Computers and Geotechnics* 73, 1–15.
- [45] Vitel, M., Rouabhi, A., Tijani, M., Guérin, F., 2016. Thermo-hydraulic modeling of artificial ground freezing: Application to an underground mine in fractured sandstone. *Computers and Geotechnics* 75, 80–92.
- [46] Wan, X., Lai, Y., Wang, C., 2015. Experimental study on the freezing temperatures of saline silty soils. *Permafrost and Periglacial Processes* 26 (2), 175–187.
- [47] Whitaker, S., 2013. *The method of volume averaging*. Vol. 13. Springer Science & Business Media.
- [48] Wu, D., Lai, Y., Zhang, M., 2017. Thermo-hydro-salt-mechanical coupled model for saturated porous media based on crystallization kinetics. *Cold Regions Science and Technology* 133, 94–107.
- [49] Wu, D., Yang, Y., Zhou, X., Wang, Y., 2019. An experimental study of heat and mass transfer in deformable sulfate saline soil during freezing. *Heat and Mass Transfer*, 1–9.
- [50] Zeng, Q., Fen-Chong, T., Li, K., 2014. Freezing behavior of cement pastes saturated with nacl solution. *Construction and Building Materials* 59, 99–110.
- [51] Zhang, Y., Michalowski, R. L., 2015. Thermal-hydro-mechanical analysis of frost heave and thaw settlement. *Journal of Geotechnical and Geoenvironmental Engineering* 141 (7), 04015027.
- [52] Zhou, J., Li, D., 2012. Numerical analysis of coupled water, heat and stress in saturated freezing soil. *Cold Regions Science and Technology* 72, 43–49.
- [53] Zhou, M., Meschke, G., 2013. A three-phase thermo-hydro-mechanical finite element model for freezing soils. *International journal for numerical and analytical methods in geomechanics* 37 (18), 3173–3193.